

Supplementary Information

Cooperative promotion of electroreduction of CO to n-propanol by ^{*}CO enrichment and proton regulation

Rongxing Qiu,^a Linxiao Cui,^a Li Peng,^{*a} Olga A. Syzgantseva,^b Jiaran Li,^a Nan Fang,^a Maria A. Syzgantseva,^c Yuan Jiang,^a Jie Zhang,^d Bingxing Zhang,^e Lingzhi Ding,^a Yangyang Dong,^a Tianwei Xue,^a Cheng Li,^a Jin-Chao Dong,^a Jinyu Ye,^a Isil Akpinar,^f Shuliang Yang,^{*a} Jun Li,^{*a} Jianling Zhang,^g Jian-Feng Li,^a and Buxing Han^{*g}

^aCollege of Chemistry and Chemical Engineering, College of Energy, Xiamen University, Xiamen, 361005, Fujian, P.R. China.

^bPeoples' Friendship University of Russia, Moscow, 117198, Russia/Department of Chemistry, Lomonosov Moscow State University, Moscow, 119991, Russia.

^cDepartment of Physics, Mendeleev University of Chemical Technology, Moscow, 125047, Russia.

^dInstitute of Chemical Sciences and Engineering, École Polytechnique Fédérale de Lausanne (EPFL), 1951 Sion, Switzerland.

^eSchool of Materials Science and Engineering, Zhejiang University, Hangzhou, 310058, Zhejiang, P.R. China.

^fDepartment of Chemistry and International Institute of Nanotechnology, Northwestern University, 2145 Sheridan Road, Evanston, IL 60208, United States.

^gBeijing National Laboratory for Molecular Sciences, CAS Key Laboratory of Colloid and Interface and Thermodynamics, CAS Research/Education Center for Excellence in Molecular Sciences, Institute of Chemistry, Chinese Academy of Sciences, Beijing, 100190, P.R. China.

*Corresponding author (e-mail: li.peng@xmu.edu.cn; ysl@xmu.edu.cn; junnyxm@xmu.edu.cn; hanbx@iccas.ac.cn)

Experimental Section

Chemicals and materials

Copper (II) chloride dihydrate ($\text{CuCl}_2 \cdot 2\text{H}_2\text{O}$, AR), sodium hydroxide (NaOH, AR), potassium hydroxide (KOH, AR), potassium chloride (KCl, AR), ethanol (AR), dimethyl sulfoxide (DMSO, AR), H_2SO_4 (98%), H_2O_2 (30%), $\text{AuCl}_3 \cdot \text{HCl} \cdot 4\text{H}_2\text{O}$ (AR), Na_2SO_3 (AR), $\text{Na}_2\text{S}_2\text{O}_3$ (AR), NH_4Cl (AR), HF ($\geq 40\%$), HCl (AR), HNO_3 (AR), NH_4F (AR), acetone (AR), isopropanol (AR) and commercial CuO were obtained from Sinopharm Chemical Reagent Co., Ltd. Proton sponge (AR) was purchased from Sigma-Aldrich Co., Ltd. Deuterium oxide (D_2O , 99.9 atom% D) was provided by Energy Chemical. Al_2O_3 was purchased from Tianjin ida Technology Co., Ltd. Nafion solution (5 wt% in water and isopropanol) was obtained from Meryer (Shanghai) Chemical Technology Co., Ltd. Conductive carbon paper (hydrophobic) and Nafion 117 proton exchange membrane were purchased from Suzhou Sinero Technology Co., Ltd. CO (99.99%) was provided by Fuzhou Xinhang Industrial Gases Co., Ltd. Unless otherwise noted, deionized water ($18 \text{ M}\Omega \cdot \text{cm}^{-1}$) was used throughout this work.

Synthesis of CuO nanosheets

The synthesis of CuO nanosheets (CuO-NS) followed the procedure reported method with some modifications¹. In the synthetic process, 512 mg $\text{CuCl}_2 \cdot 2\text{H}_2\text{O}$ was dissolved in 30 mL deionized water under magnetic stirring. Whereafter, 7.2 g NaOH was dissolved in 30 mL deionized water and the above alkaline liquid was added to the aforementioned CuCl_2 aqueous solution drop by drop. The solution was stirred for 10 min and transferred into a 100 mL of Teflon-lined autoclave, sealed, and heated at 100 °C for 12 h. The system was allowed to cool to room temperature naturally, and the resulting product was centrifuged, rinsed with distilled water and ethanol several times to remove any alkaline salt. Finally, the CuO-NS was obtained by drying in a vacuum oven at 70 °C for 12 h.

Preparation of electrodes

Preparation of CuO-NS-x% PS (x = 10, 20, 30 and 50): The electrodes of CuO-NS with different proton sponge amounts (10%, 20%, 30% and 50%) were prepared accordingly. Typically, 2 mg proton sponge was dissolved in 2 mL isopropanol, then 10 mg CuO-NS catalyst and 20 μ L Nafion solution (5 wt% in water and isopropanol) were added, and the solution was sonicated for 30 min to obtain a homogeneous ink. Then, ~ 1 mg cm^{-2} CuO-NS with corresponding amounts of proton sponge were loaded on hydrophobic conductive carbon paper. The electrode was dried in a vacuum oven at 70 $^{\circ}\text{C}$ for 12 h to remove any residual solvents. Commercial CuO electrodes, both with and without proton sponge, can be obtained using the same method by substituting the CuO-NS with commercial CuO precursor, respectively. Preparation of Cu-NS-after 20% PS: The CuO-NS was first *in situ* reduced at -0.44 V vs. RHE for 30 min, then 20% proton sponge was introduced on Cu-NS catalyst surface.

Materials characterization

PXRD was recorded on Rigaku Smart Lab-SE powder X-ray diffractometer with Cu $K\alpha$ radiation ($\lambda = 1.5418$ \AA) at room temperature. Raman measurements were carried out with a XploRA Plus instrument. The infrared spectrum of samples was measured by Thermo Scientific Nicolet iS50 FT-IR spectrometer. SEM images were acquired using field emission scanning electron microscope of ZEISS Sigma. The morphology, lattice distance and the EDX elemental mappings of the catalysts were measured on FEI Tecnai F30 transmission electron microscope at an acceleration voltage of 300 kV. XPS measurements were implemented on Thermo Escalab 250Xi spectrometer using a photon energy of 461 eV with an energy resolution of 0.1 eV. TGA of proton sponge-modified CuO and their controlled sample were obtained by a NETZSCH TG 209 F1 Libra between 30 $^{\circ}\text{C}$ with 400 $^{\circ}\text{C}$ by a heating ratio of 10 $^{\circ}\text{C}/\text{min}$ under a N_2/O_2 atmosphere.

CO electroreduction measurement under different CO pressures

CO electrolysis under different pressures was operated in a custom-made pressurized cell with two-compartment PEEK lining separated by a Nafion 117 proton exchange membrane. Pressure resistant quartz windows for observation of electrochemical system were equipped in the high-pressure cell, and PEEK lining with a three-electrode system was connected to an electrochemical workstation instrument (CHI 660E). Pt mesh and Hg/HgO (1 M KOH) were used as the counter electrode and the reference electrode, respectively. 36 mL of 1 M KOH solution was used as the electrolyte in each compartment. For the CO electrolysis under elevated CO pressure, the electrolytes both in the cathode and anode were bubbled with CO for at least 30 min to remove the dissolved air before pressurization. Subsequently, CO was charged into the pressured cell equipped with digital pressure gauge and the flow rate was controlled by a micro-regulation valve. For the CO electrolysis under ambient pressure, the electrolyte in the cathode was bubbled with CO at the rate of 20 mL min⁻¹ for 30 min to form a CO-saturated solution before CO reduction testing. For the CO electrolysis under 0.5 bar CO pressure, the electrolyte in the cathode was bubbled with CO at the rate of 10 mL min⁻¹ and Ar at the rate of 10 mL min⁻¹ for 30 min to form a CO-saturated solution before CO reduction testing. In all measurements, Hg/HgO (1 M KOH) was used as the reference electrode. The potential E was measured against a Hg/HgO reference electrode (1 M KOH) and converted to V vs. RHE using

$$E (\text{vs. RHE}) = E (\text{vs. Hg/HgO}) + 0.140 \text{ V} + 0.0591 \times \text{pH} (1 \text{ M KOH, pH} = 13.8)$$

CO electroreduction product analysis

To quantify the gas products during electrolysis under ambient CO pressure, CO gas (MESSER gas, $\geq 99.99\%$) was delivered into the cathodic compartment at a rate of 20.0 standard cubic centimeters per minute (sccm, monitored by Sevenstar mass flow controller) and vented into a GC (GC, FULI instruments GC-9790II) equipped with a combination of 10% OV-1, Porapak N, and TDX-01 columns. A thermal conductivity detector (TCD) was mainly used to quantify H₂ concentration, and a flame ionization

detector (FID) with a methanizer was used to quantitative analysis hydrocarbon species. For high-pressure CO electroreduction test, CO was charged into both the cathodic and anodic compartments of the cell, which was equipped with a digital pressure gauge. The flow rate was controlled by a micro-regulation valve. After the CORR test, the remaining CO and gas products were decompressed into gas bags. A controlled amount of the gas products was then injected into the GC for gas product analysis via a gas-phase injection needle. The liquid products were detected by the ^1H NMR spectroscopy (Bruker AVANCE AV III 500), where DMSO was used as the reference standard, D_2O and H_2O were used as the lock solvent. The Faradaic efficiency (FE) values of different CORR products under both ambient pressure and high pressure were calculated as follows:

$$FE = \frac{n \times F \times \text{amount of product}}{Q} \times 100\%$$

where n is the number of moles of electrons to participate in the faradaic reaction, F is the Faraday constant (96485 C/mol), and Q is the amount of charge passed through the working electrode.

Electrochemical Impedance Spectroscopy (EIS) measurement

The EIS measurement was carried out in 1 M KOH solution at an open circuit potential (OCP) with an amplitude of 5 mV of 10^{-2} to 10^6 Hz.

Electrochemical active surface areas (ECSA) measurement

The electrochemical active surface area is proportional to C_{dl} value. C_{dl} was determined by measuring the capacitive current associated with double-layer charging from the scan-rate dependence of cyclic voltammogram (CV). In a typical procedure, the catalysts were reduced via linear sweep voltammetry (LSV) with a scan speed of 20 mV s^{-1} over a potential range from OCP to -0.64 V vs. RHE . In order to avoid CO and OH^- adsorption on the catalyst surface affecting the test results, Ar and 0.1 M KClO_4 were used as the test atmosphere and electrolyte, respectively. Pt mesh and Ag/AgCl (saturated KCl) were used as the counter electrode and the reference

electrode, respectively. The CV ranged from non-Faradaic region -0.076 V to 0.024 V vs. RHE. The C_{dl} was estimated by plotting $\Delta j (j_a - j_c)$ at -0.026 V vs. RHE against the scan rates, in which j_a and j_c were the anodic and cathodic current density, respectively. The scan rates were 10, 20, 30, 40 and 50 mV s^{-1} . In order to decrease the data error in the experiment, we have tested the cyclic voltammetry curve of Cu-NS-x% PS ($x = 0, 10, 20, 30,$ and 50) three times and fit the C_{dl} value with an error bar of the standard deviation of three independent measurements (Table S3). The potential E was measured against an Ag/AgCl reference electrode (saturated KCl) and converted to V vs. RHE using

$$E(\text{vs. RHE}) = E(\text{vs. Ag/AgCl}) + 0.210 \text{ V} + 0.0591 \times \text{pH} (0.1 \text{ M KClO}_4, \text{pH} = 7.0)$$

***In situ* Raman spectroscopy experiment**

In situ Raman measurements were carried out with a XploRA Plus instrument using a 638 nm excitation laser and signals were recorded using 60 s integration in a customized-made high pressure *in situ* Raman cell setup with a three-electrode. The catalyst on glassy carbon, Pt mesh and Hg/HgO (1 M KOH) were used as the work electrode, the counter electrode and the reference electrode, respectively. The laser power was 10 mW, and the objective (Olympus, $\times 50$) was used. Before collecting the spectra, all electrodes were electrochemically reduced by LSV. The CORR test was performed at the potential of -0.44 V vs. RHE and the Raman signals were collected synchronously.

***In situ* ATR-SEIRAS experiment**

The Cu-NS and the Cu-NS-20% PS electrodes under ambient CO pressure and 3 bar CO for ATR-SEIRAS investigation were prepared on Au film that was predeposited onto a silicon ATR crystal by chemical deposition, which was a slight modification of that reported by Osawa et al.². Specifically, the silicon prism was mechanically polished using a $0.05 \mu\text{m}$ Al_2O_3 slurry and sonicated in acetone and water to remove any residue Al_2O_3 particles. After polishing, the silicon prism was immersed in a 7:3

by volume solution of H₂SO₄ (98%) and H₂O₂ (30%) for 20 min to remove possible organic contaminants on the prism. Following that, the reflecting plane of the prism was immersed in NH₄F solution (40%) for 40-60 s to remove the surface oxides as well as create a hydrogen-terminated surface for improving the adhesion of the Au film. The Au film was then chemically deposited by immersing the reflecting surface in a 1:1:1 by volume mixture of 30 mM HAuCl₄·4H₂O solution, plating solution consisting of 0.3 M Na₂SO₃, 0.1 M Na₂S₂O₃, 0.1 M NH₄Cl and 2% HF. The electrode was prepared by dropping the catalyst ink suspension onto the Au film. A customized single-compartment, three-electrode spectroelectrochemical pressurized cell was employed for the *in situ* SEIRAS test. The cell was assembled on a Nicolet 8700 FT-IR spectrometer equipped with a liquid nitrogen-cooled MCT detector and connected to an electrochemical workstation. All spectra were collected at an 8 cm⁻¹ spectral resolution during stepping the working electrode potential. In a typical process, the catalyst-deposited Si prism was used as the working electrode with a Pt wire as the counter electrode and Hg/HgO (1 M KOH) as the reference electrode. Before collecting the spectra, all electrodes were electrochemically reduced by LSV and the background was then placed at OCP in CO-saturated 0.1 M KOH (pH 13).

The resulting spectra were reported as relative change in reflectivity:

$$\frac{\Delta R}{R} = \frac{R(E_S) - R(E_R)}{R(E_R)}$$

Where $R(E_S)$ and $R(E_R)$ are single-beam spectra collected at the sample potential and the reference potential, respectively.

DFT calculations

The simulations were performed within the Density Functional theory (DFT) using Perdew-Burke-Ernzerhof (PBE)³ density functional, as implemented within Quantum Espresso ab initio simulation package⁴. To represent the wavefunction and electron density a plane wave basis set with 40 Ry and 240 Ry kinetic energy and charge density cutoffs, respectively, was employed. Core electron region and core-valence interactions were described using Vanderbilt ultrasoft pseudopotentials⁵. The 8×8×8

and $2 \times 2 \times 1$ Γ -centered k-point meshes were employed for the relaxation of bulk and surface structures, respectively. The bulk models of Cu and Cu₂O were fully relaxed both in terms of lattice parameters and atomic positions and after that (111) surface slabs of each type were cut out from these models. The Cu⁰/Cu⁺ model was represented by a partially reduced Cu₂O oxide (111) surface model having oxygen surface vacancies within it, that represented a situation of the Cu⁰/Cu⁺ layer. Each surface contained 4 layers in z-direction and was represented by a 2×2 supercell. The vacuum of at least 12 Å was ensured for each slab model. The oxygen formation energy was calculated as follows:

$$\Delta_f E = E_{surf+Ovac} - E_{surf} - \frac{1}{2}E_{O_2}$$

While the adsorption energies of *OCCO and *OCCOCO species were calculated using the following formula:

$$E_{ads} = E_{surf+mol} - E_{surf} - nE_{CO}$$

Where E_{surf} , $E_{surf+Ovac}$, $E_{surf+mol}$ and E_{CO} stand for adsorption energies of the pristine surface, the surface having oxygen vacancy, the surface having vacancies of the adsorbate, and *CO, respectively.

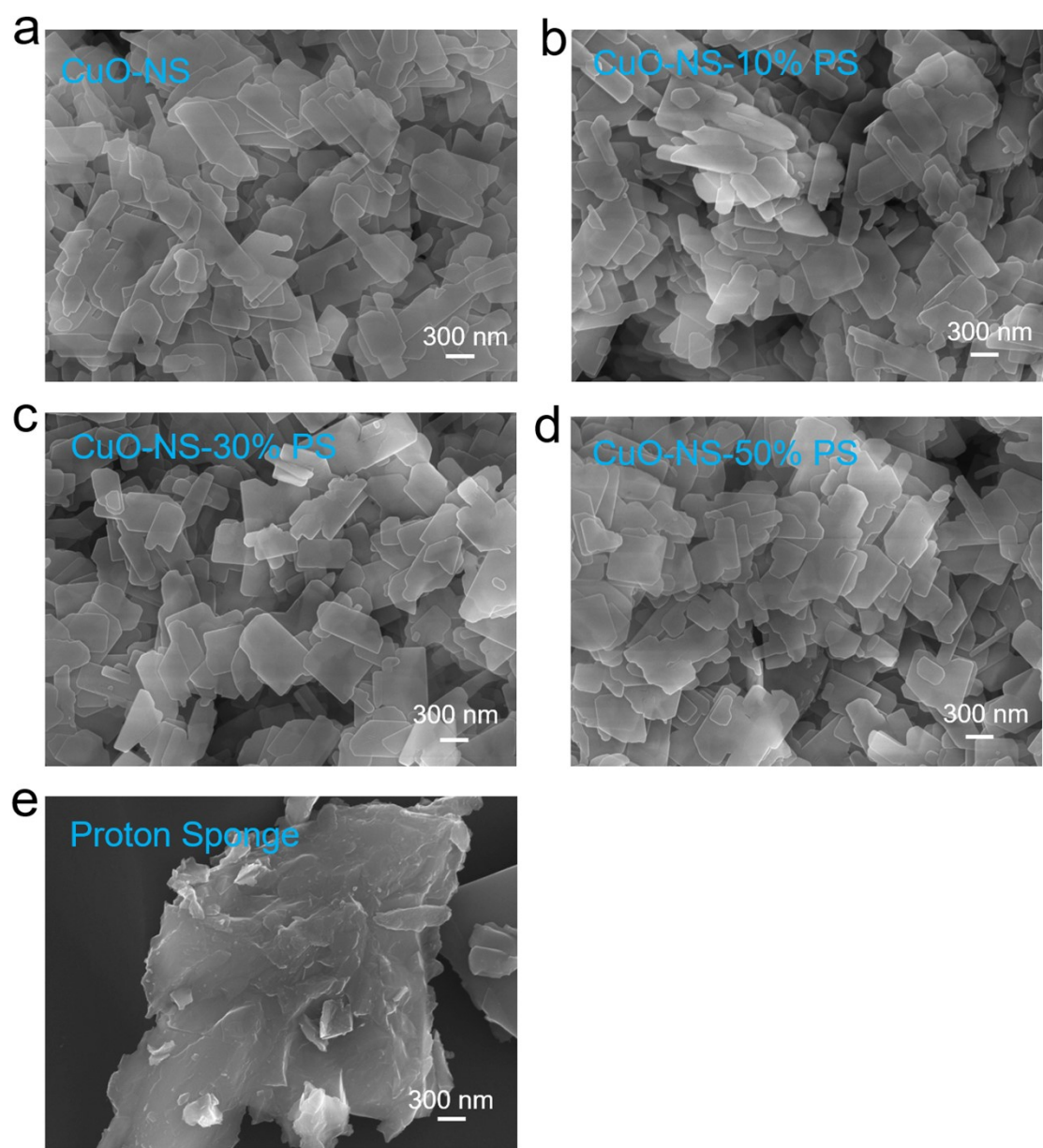


Fig. S1. SEM images of CuO-NS-x% PS (x = 0, 10, 30 and 50) with different proton sponge amounts and pure proton sponge.

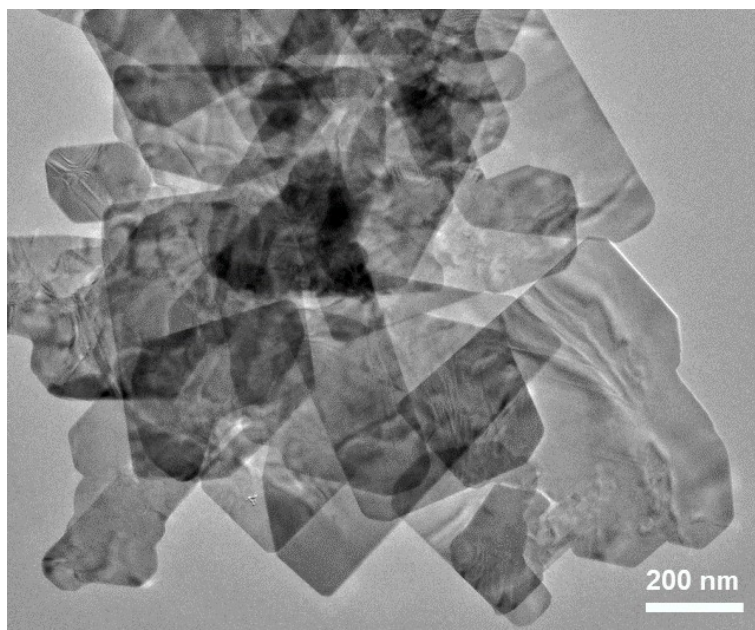


Fig. S2. Low magnification TEM image of CuO-NS.

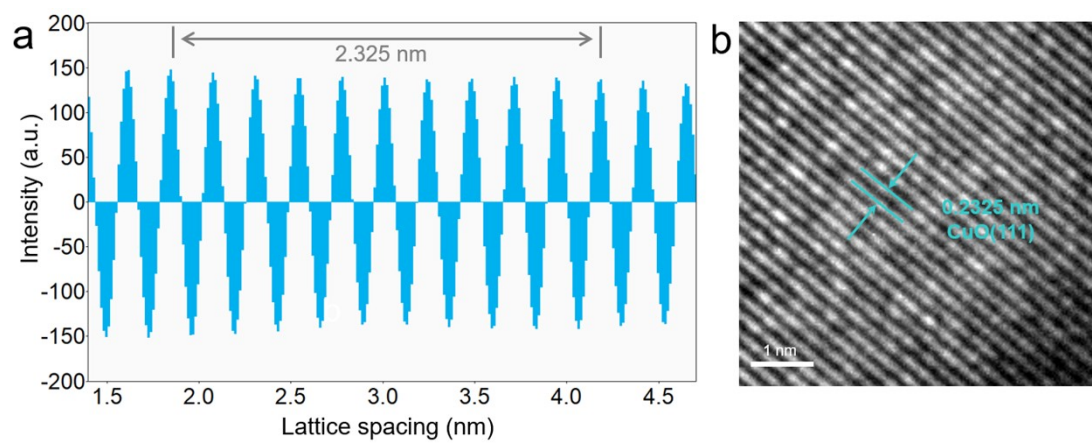


Fig. S3. (a) Intensity profile measured from the cyan region marked in Fig. 1d. (b) IFFT pattern of CuO-NS-20% PS.

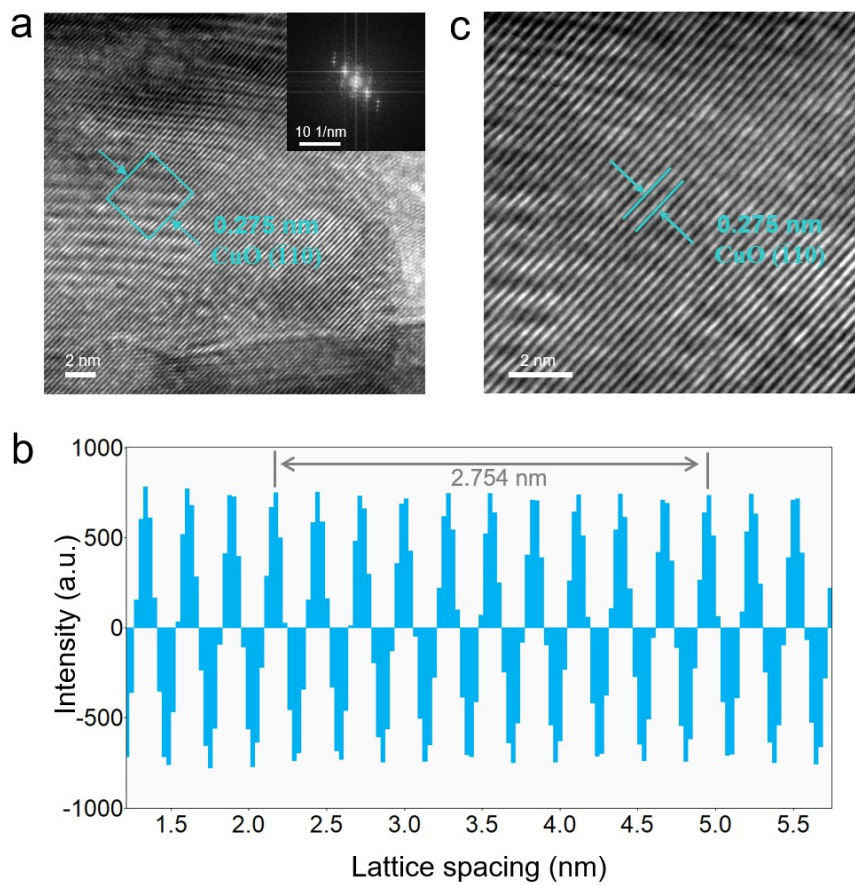


Fig. S4. HRTEM characterization of Cu-NS. (a) HRTEM images of CuO-NS and the corresponding FFT pattern (inset). (b) The corresponding intensity profiles measured from the cyan region marked in image (a). (c) IFFT pattern of CuO-NS.

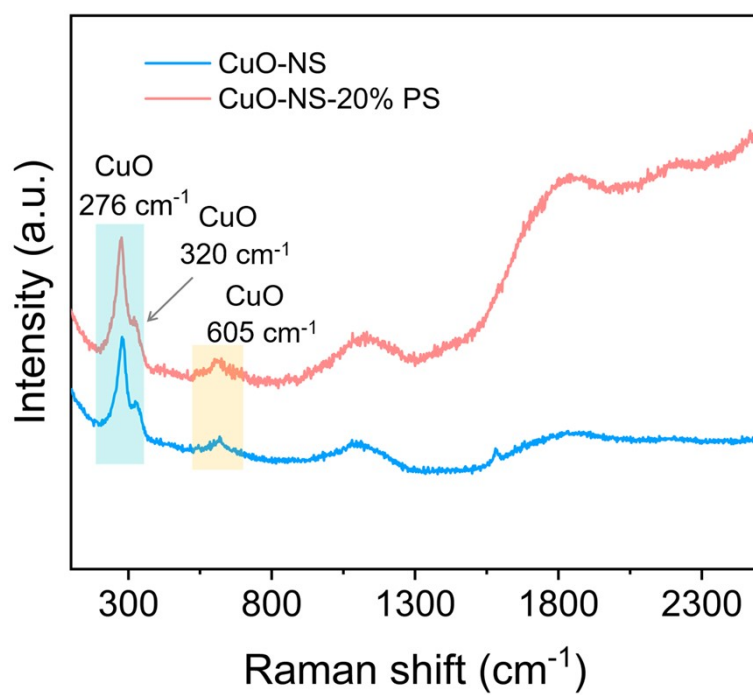


Fig. S5. Raman spectra of CuO-NS and CuO-NS-20% PS.

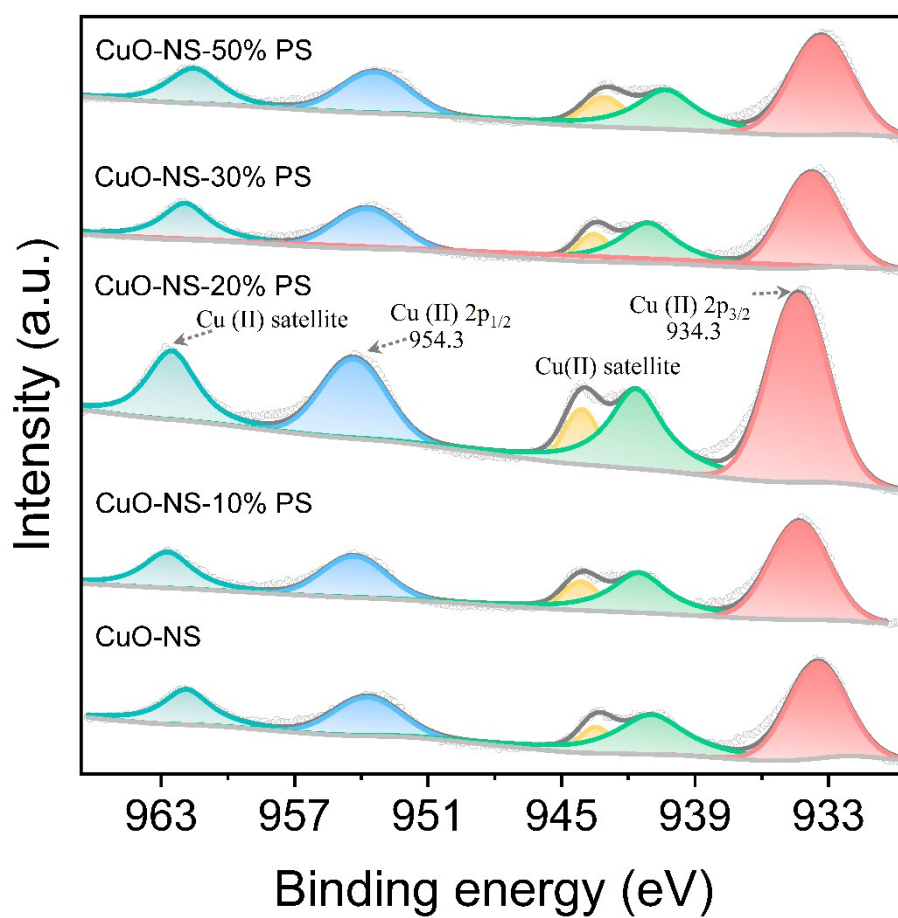


Fig. S6. XPS spectra of Cu 2p for CuO-NS-x% PS (x = 0, 10, 20, 30 and 50).

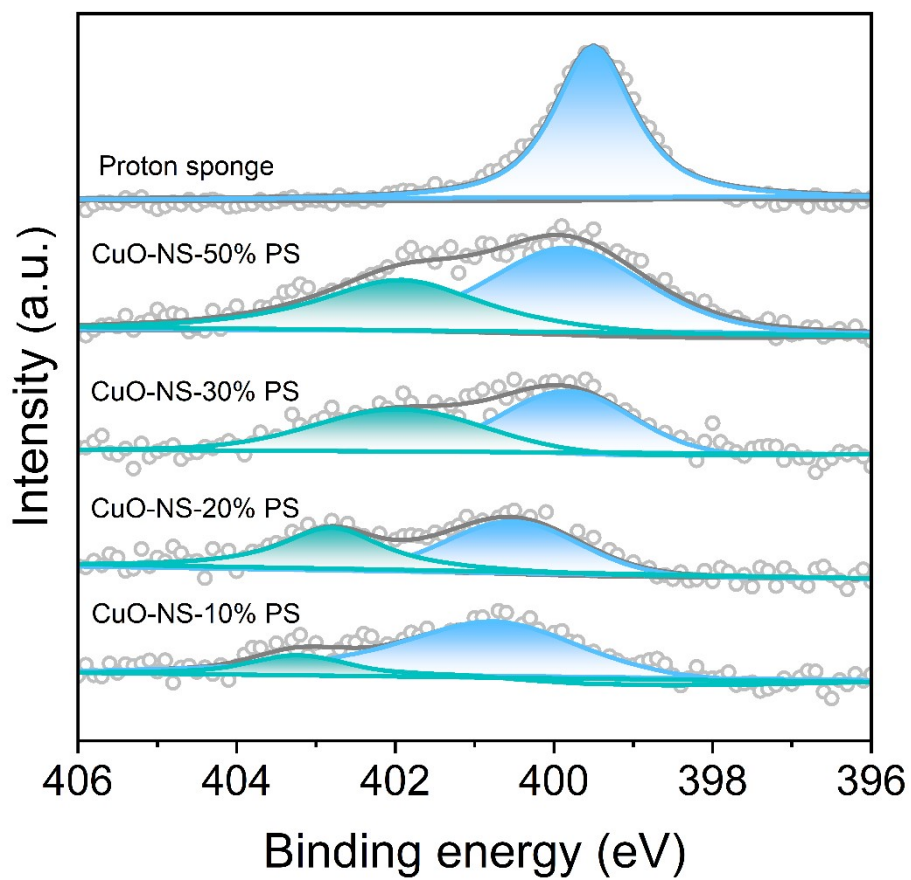


Fig. S7. XPS spectra of N 1s for pure proton sponge and CuO-NS-x% PS (x = 10, 20, 30 and 50).

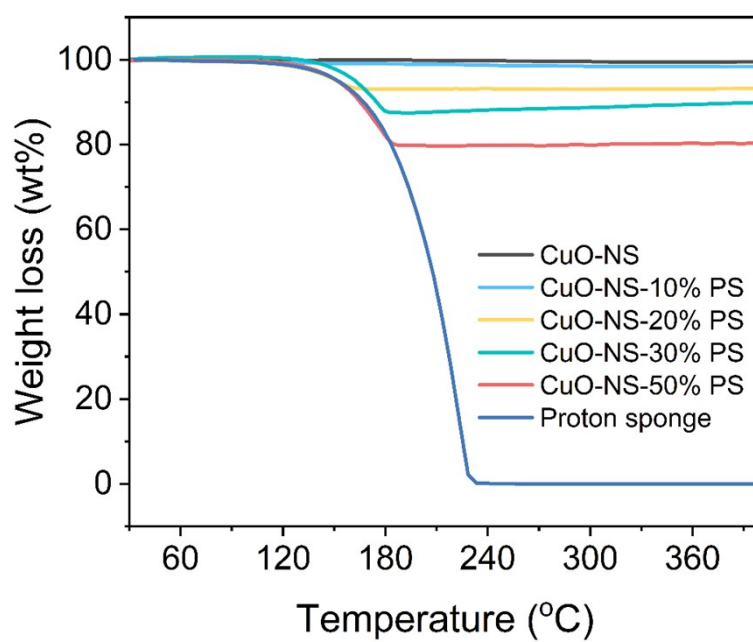


Fig. S8. TGA plot of CuO-NS-x% PS (x = 0, 10, 20, 30 and 50) and proton sponge with temperature increase from 30 °C to 400 °C with increase ratio as 10 °C/min under N₂/O₂ atmosphere.

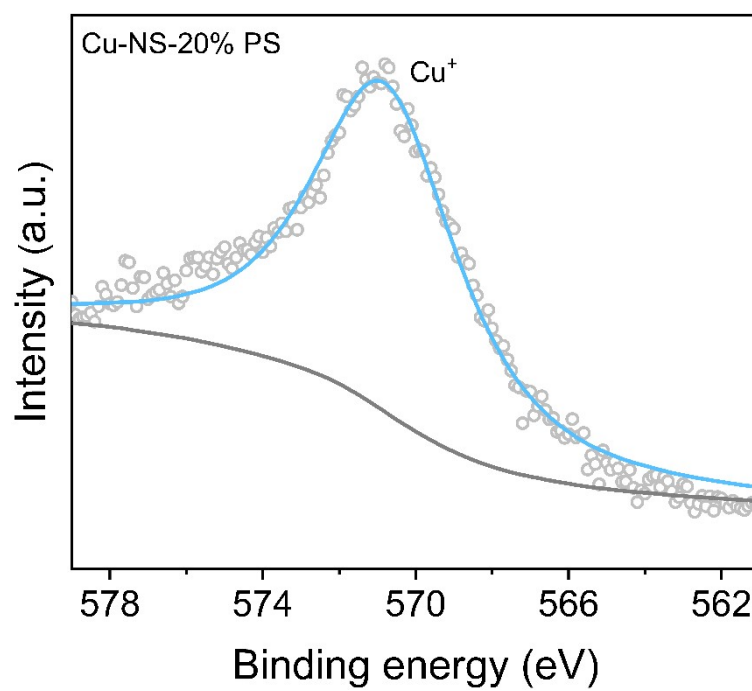


Fig. S9. Cu LMM Auger spectra of Cu-NS-20% PS after electroreduction pretreatment.

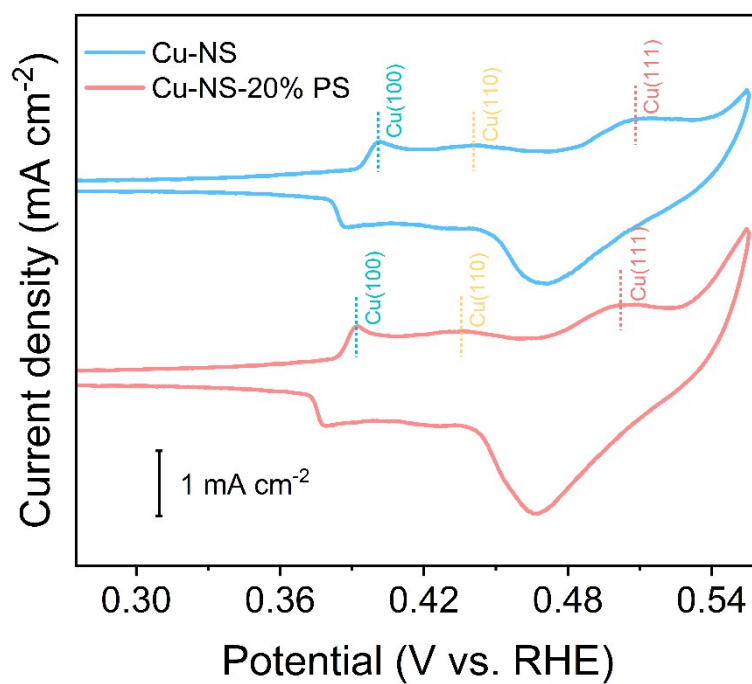


Fig. S10. CV curves of Cu-NS (blue) and Cu-NS-20% PS (red) in 1 M KOH under Ar atmosphere. Scan rate: 20 mV s⁻¹.

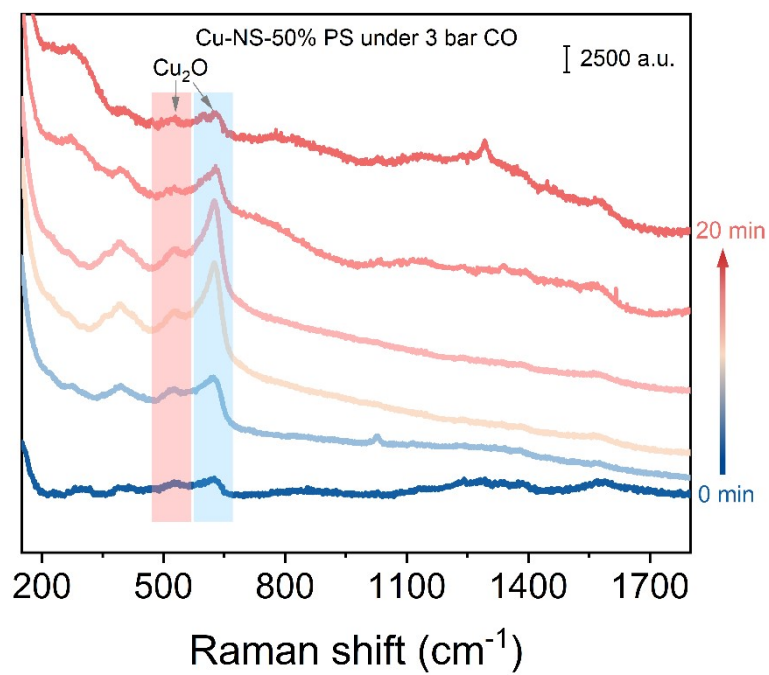


Fig. S11. *In situ* Raman spectra of Cu-NS-50% PS under 3 bar CO at -0.44 V vs. RHE.

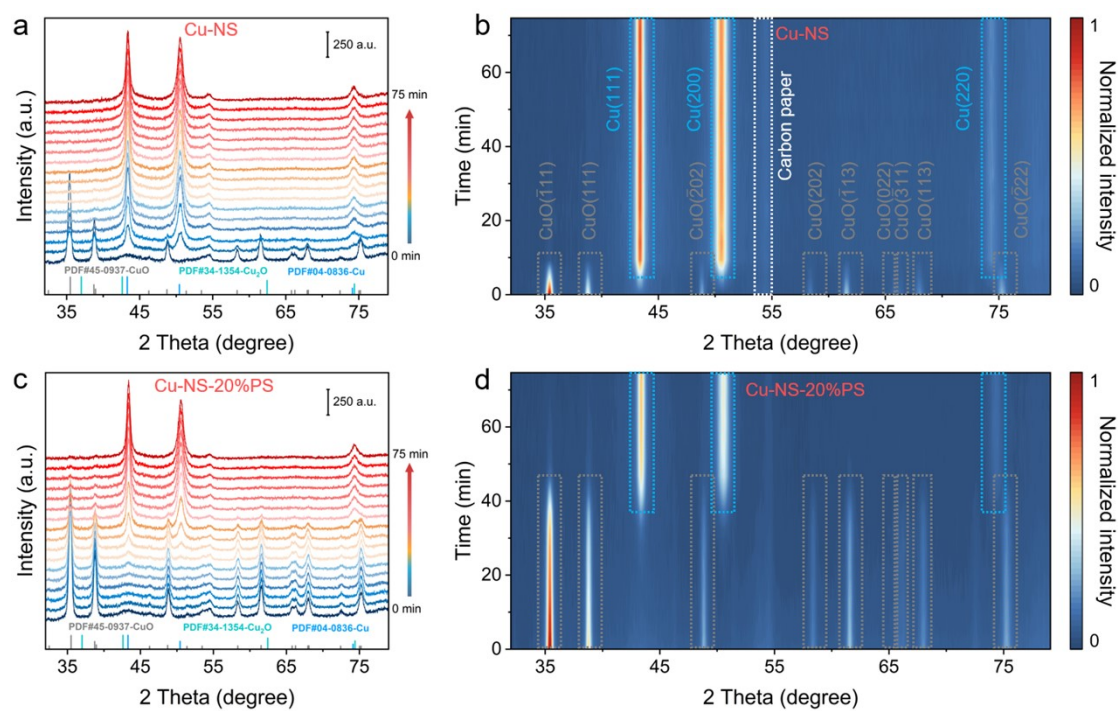


Fig. S12. *In situ* XRD patterns of Cu-NS and Cu-NS-20% PS during CORR under ambient CO pressure.

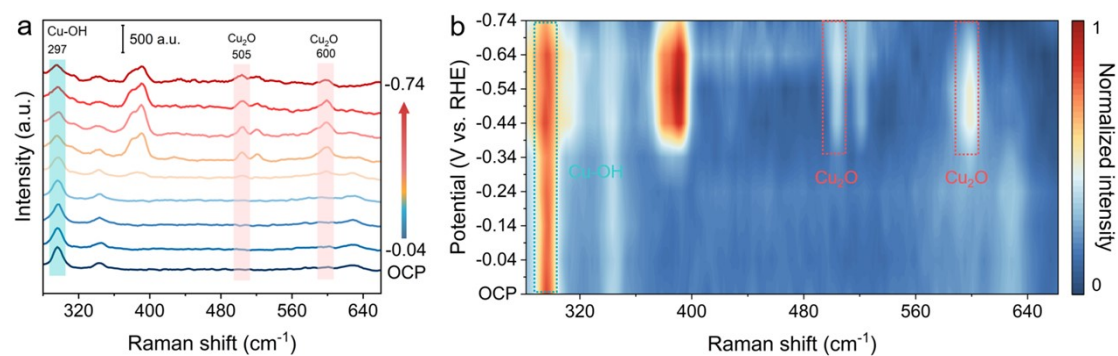


Fig. S13. *In situ* Raman spectra of Cu-NS during CORR under ambient CO pressure.

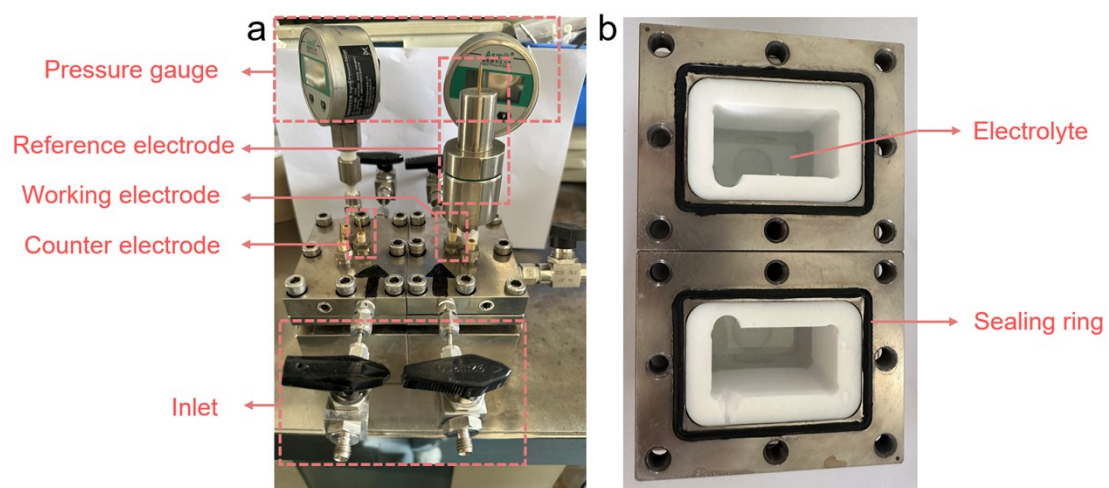


Fig. S14. Photographs of the (a) pressurized electrolysis setup and the (b) electrolysis cell.

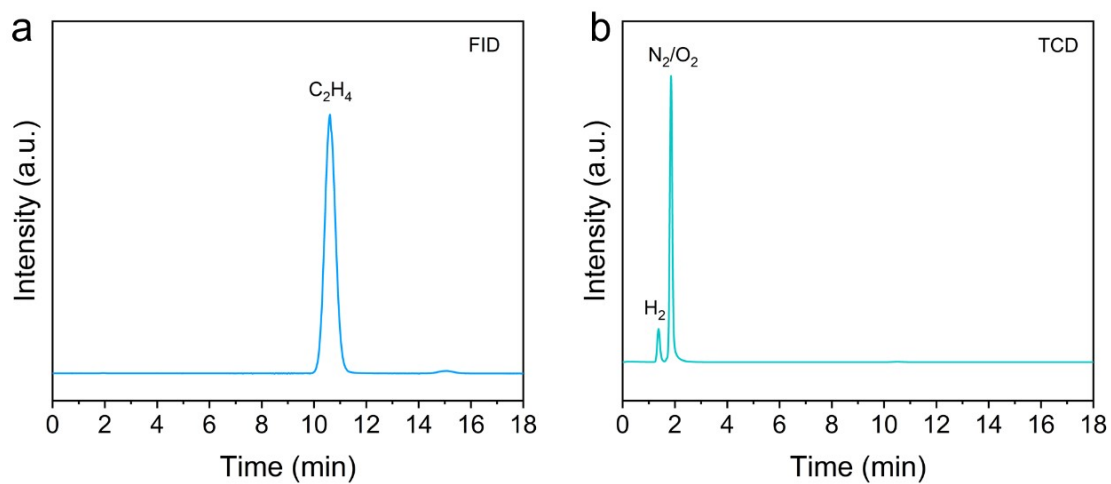


Fig. S15. Typical gas-chromatographic traces of gaseous products after electrolysis with the Cu-NS-20% PS catalyst.

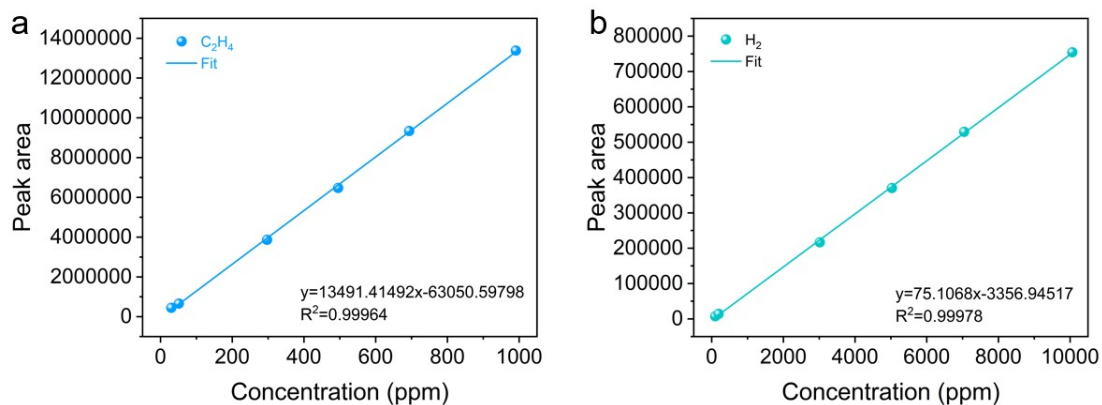


Fig. S16. Calibration curves for (a) C_2H_4 and (b) H_2 components in gas chromatography, respectively.

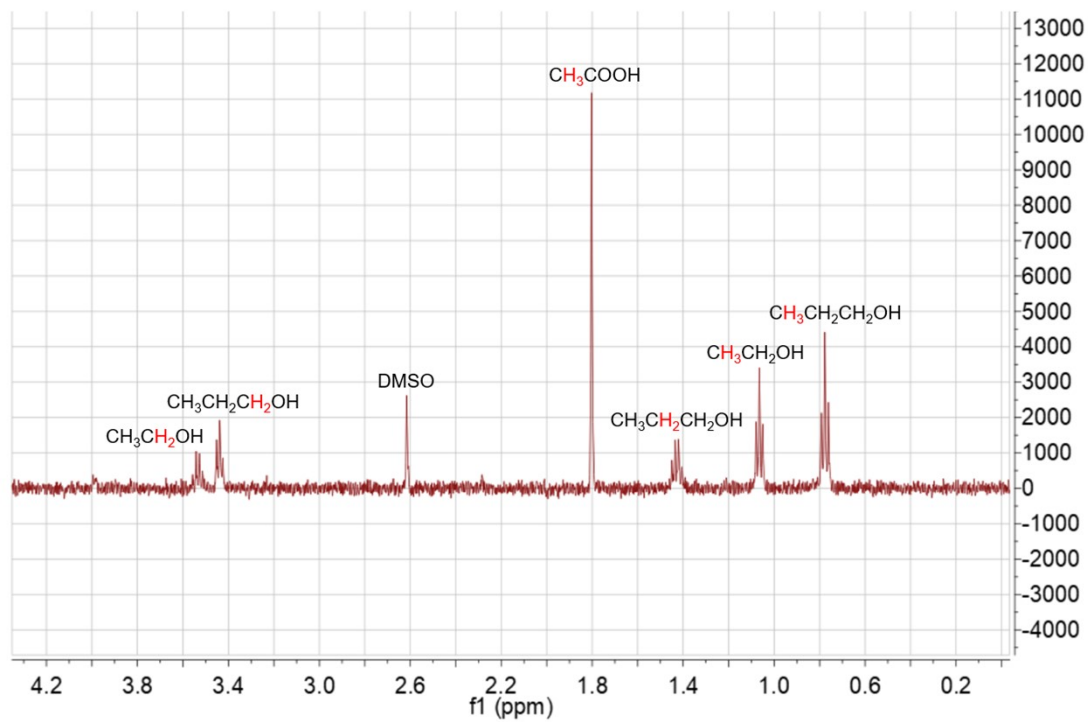


Fig. S17. A typical ^1H NMR spectrum of liquid products after electrolysis with the Cu-NS-20% PS catalyst.

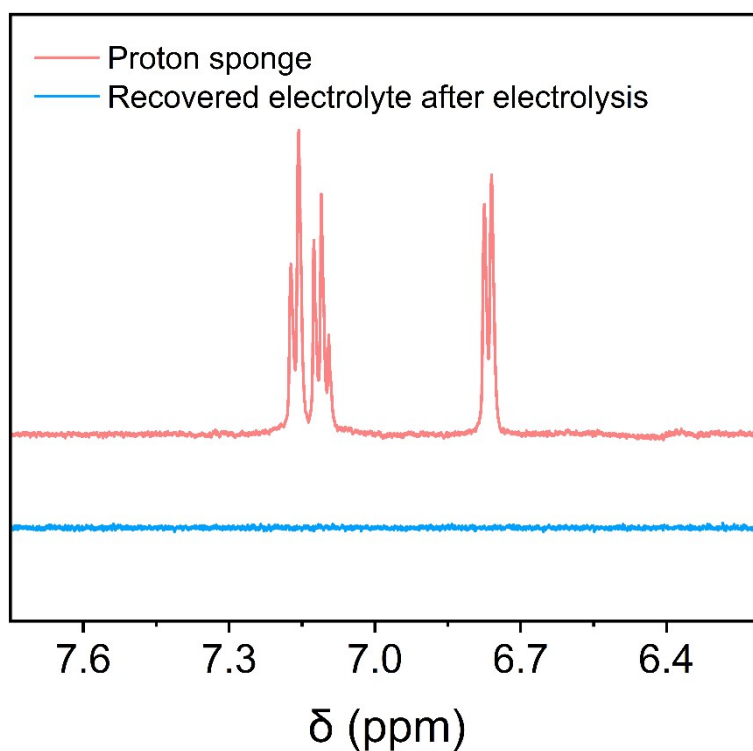


Fig. S18. Comparison of the ¹H NMR spectrum (500 MHz, D₂O, 298 K) of the proton sponge dissolved in isopropanol and 1 M KOH aqueous solution with a typical ¹H NMR spectrum of the liquid products after electrolysis using the Cu-NS-20% PS catalyst.

After CORR, no signals from proton sponge were detected in the ¹H NMR spectrum of the recovered electrolyte (Fig. S17), which indicated that the water-insoluble proton sponge was resistant to be replaced by the reaction species during the CORR process in aqueous electrolyte.

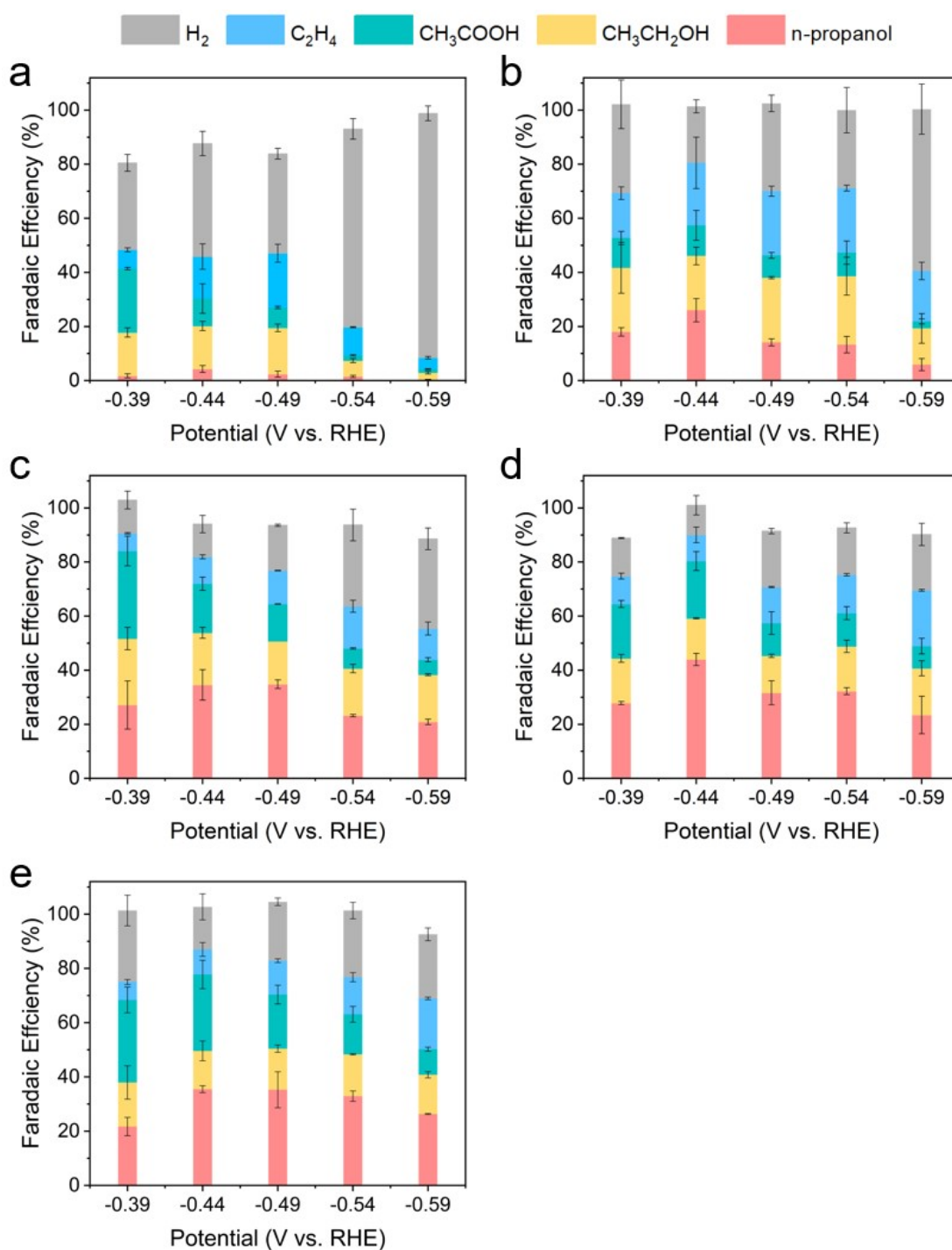


Fig. S19. CORR product distributions for (a) Cu-NS-20% PS under 0.5 bar CO, (b) Cu-NS-20% PS under 1 bar CO, (c) Cu-NS-20% PS under 2 bar CO, (d) Cu-NS-20% PS under 3 bar CO and (e) Cu-NS-20% PS under 5 bar CO.

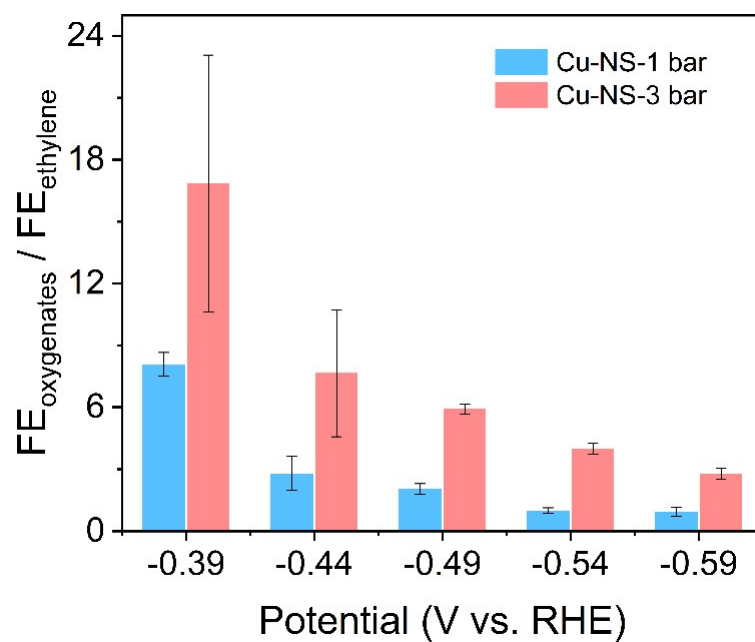


Fig. S20. The comparison of $FE_{\text{oxygenates}}/FE_{\text{ethylene}}$ ratios on Cu-NS under different CO pressures (1 bar vs. 3 bar CO).

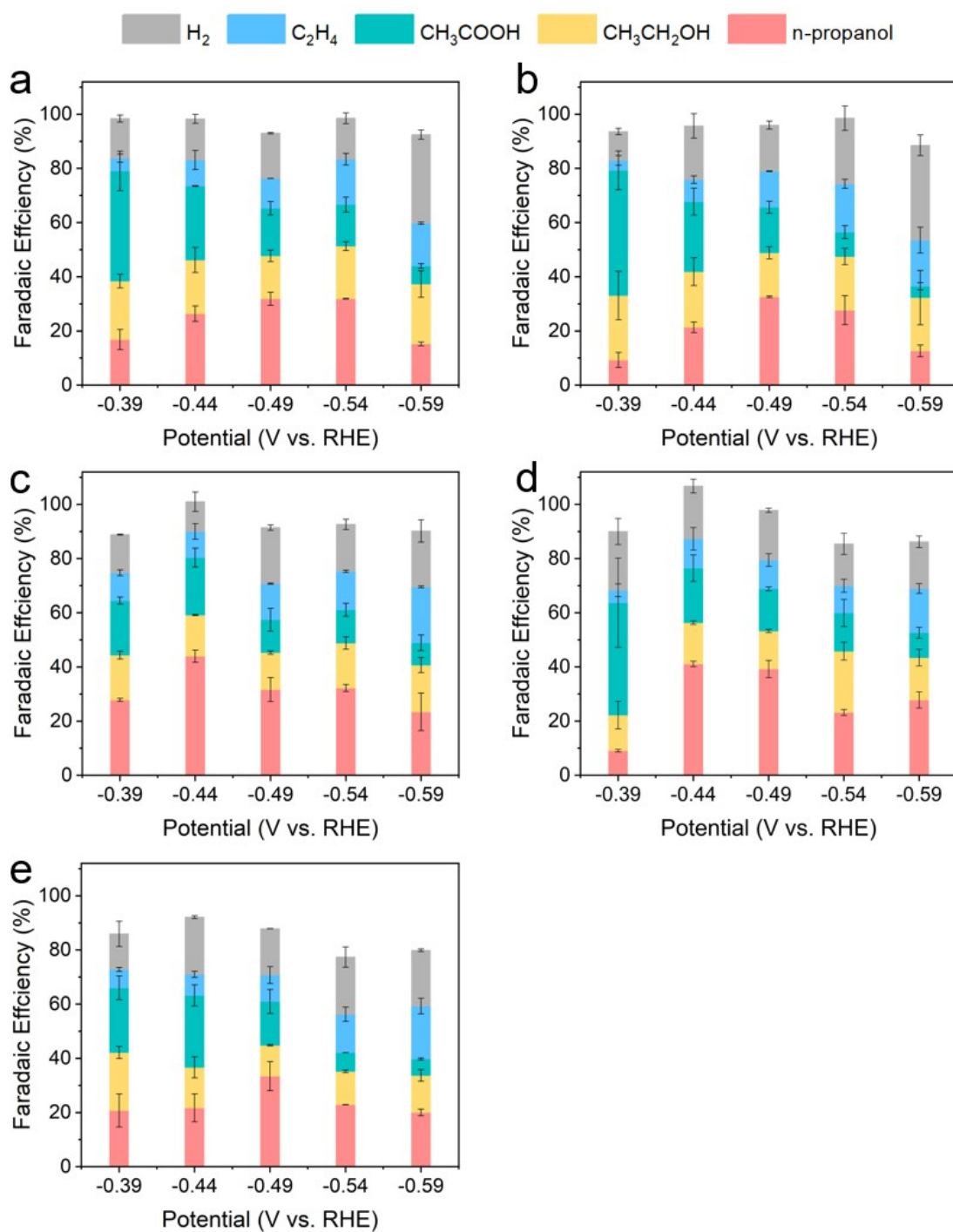


Fig. S21. CORR product distributions for (a) Cu-NS (b) Cu-NS-10% PS (c) Cu-NS-20% PS (d) Cu-NS-30% PS (e) Cu-NS-50% PS under 3 bar CO.

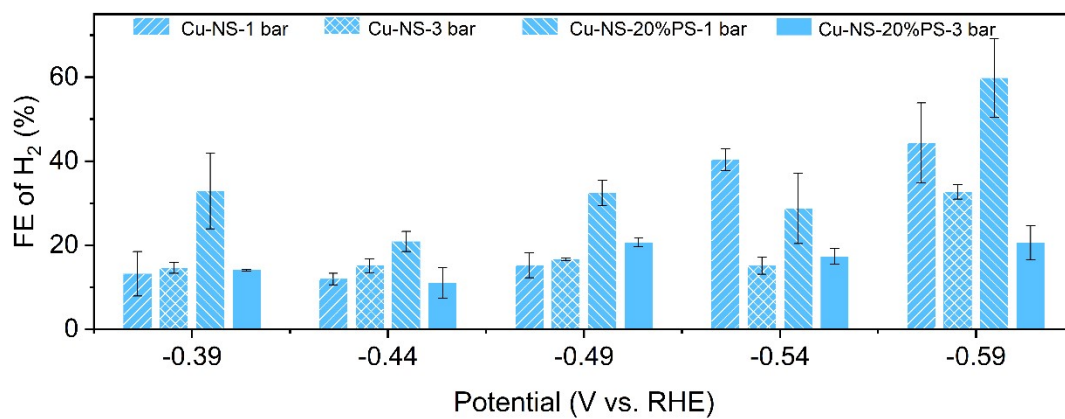


Fig. S22. FE of H₂ for Cu-NS and Cu-NS-20% PS under 1 bar and 3 bar CO, respectively.

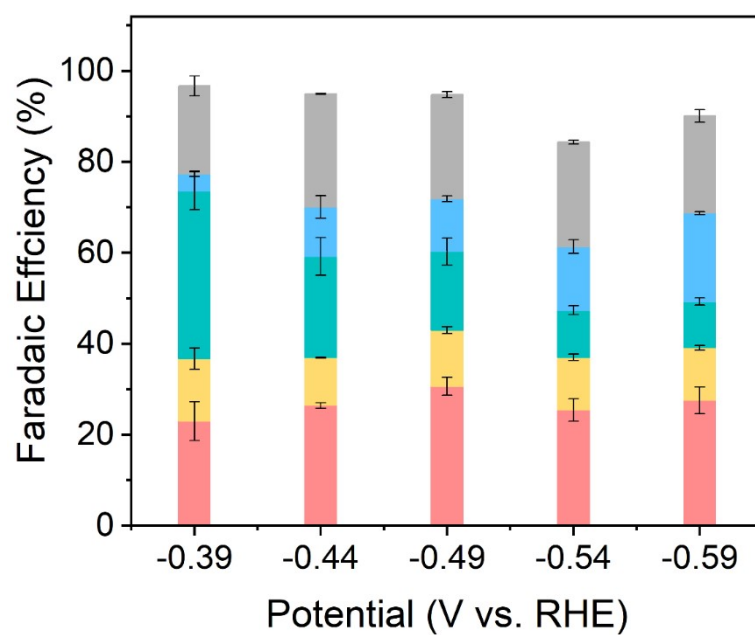


Fig. S23. CORR product distributions for Cu-NS-30% PS under 5 bar CO.

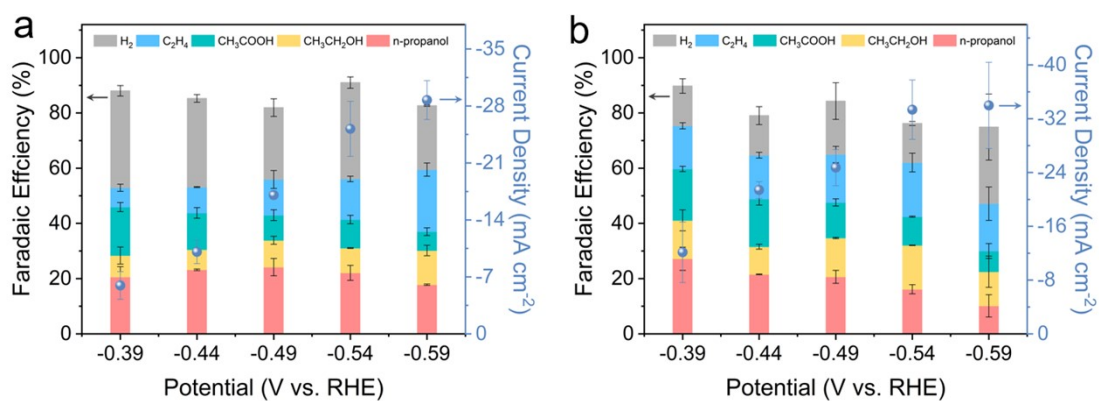


Fig. S24. CORR product distributions and total current density for Cu-NS-20% PS under 3 bar CO with (a) 0.5 M KOH and (b) 2 M KOH as electrolyte, respectively.

In this comparative study of KOH concentration effects on CORR performance, we systematically modulated only the KOH concentration while keeping other experimental parameters constant. This controlled approach ensured that any observed variations were unambiguously attributable to alkaline conditions, without interference from extraneous ions.

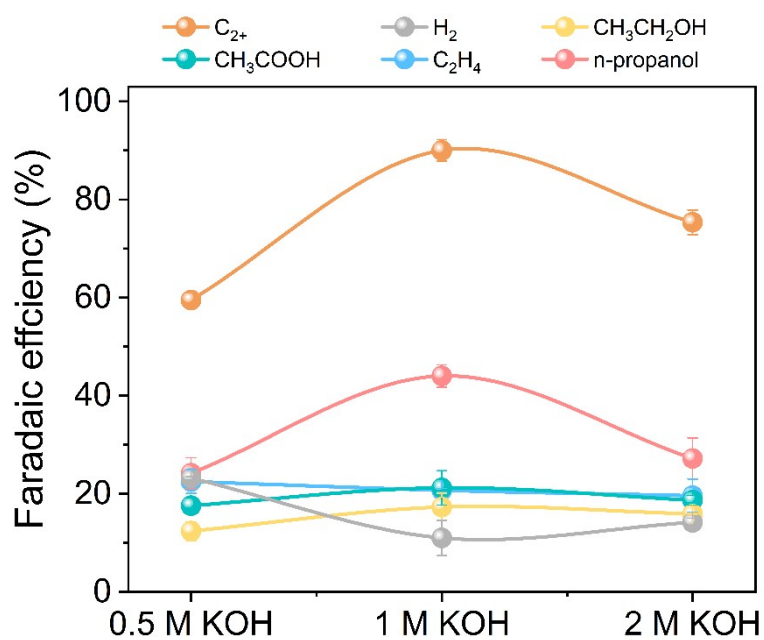


Fig. S25. Product distributions of H₂, CH₃CH₂OH, CH₃COOH, C₂H₄, n-propanol and C₂₊ products of Cu-NS-20% PS in CORR under 3 bar CO pressure at different KOH concentrations.

The FE of n-propanol and H₂ exhibit significant variations (FE_{n-propanol} peaks while FE_{H₂} minimizes in 1 M KOH), whereas FE of ethylene, ethanol, and acetate remain largely unaffected.

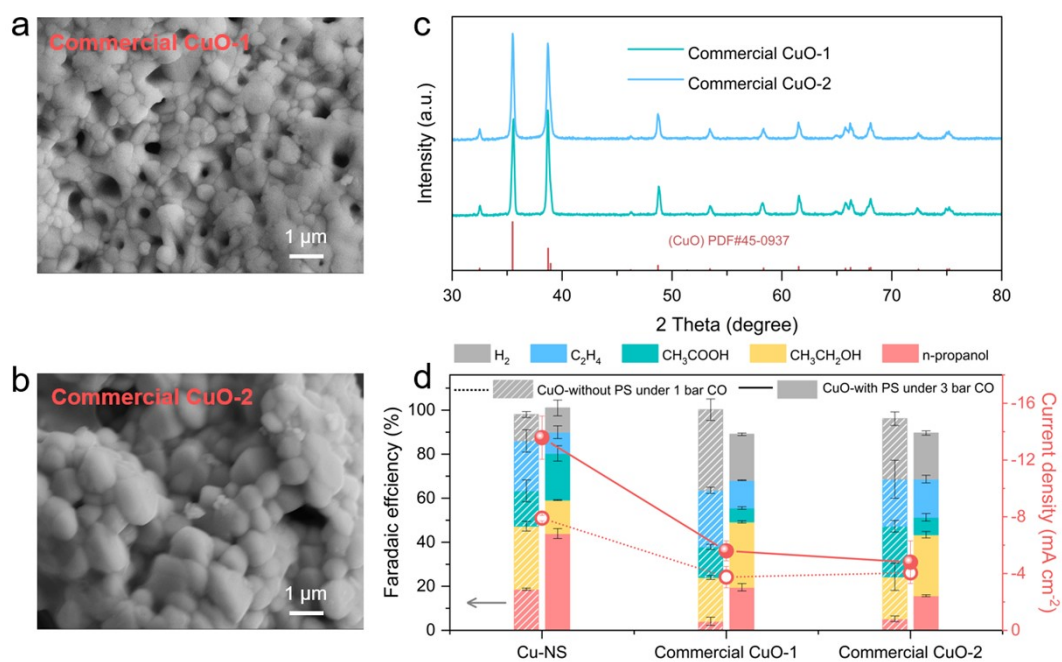


Fig. S26. Characterizations and CORR performance of different CuO-based samples. SEM images (a-b) and XRD patterns (c) of two commercial CuO. (d) CORR performance of three CuO-based catalysts without PS under 1 bar CO and with PS under 3 bar CO at -0.44 V vs. RHE.

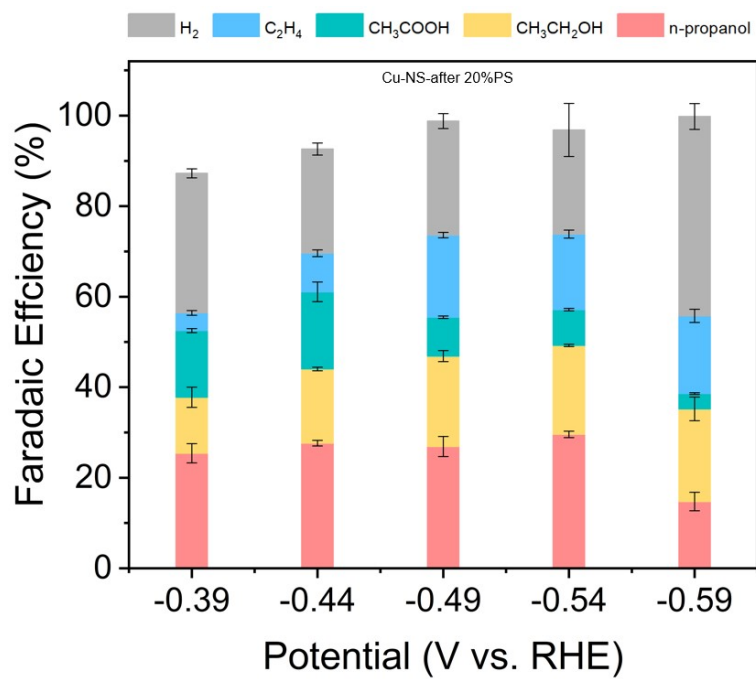


Fig. S27. CORR product distributions of Cu-NS-after 20% PS under 3 bar CO.

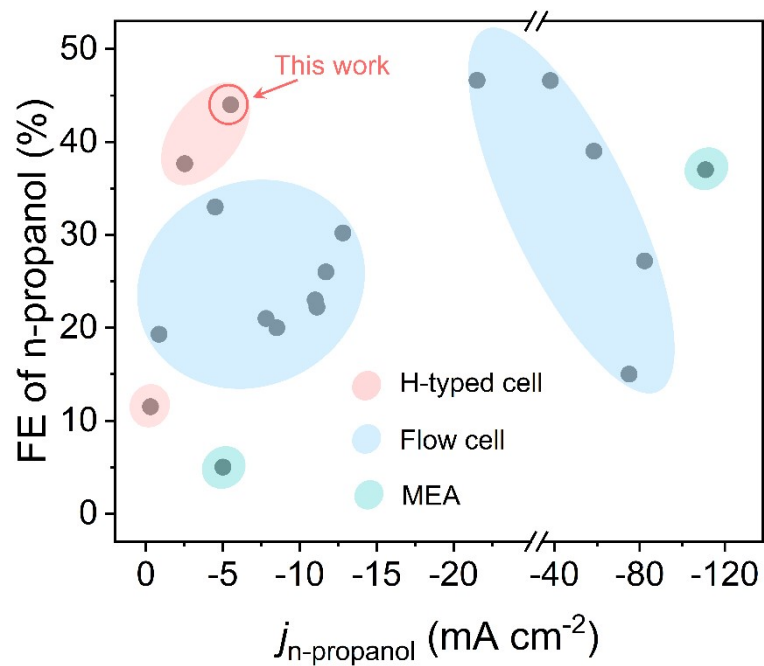


Fig. S28. $\text{FE}_{n\text{-propanol}}$ vs. $j_{n\text{-propanol}}$ for various Cu-based catalysts in CORR.

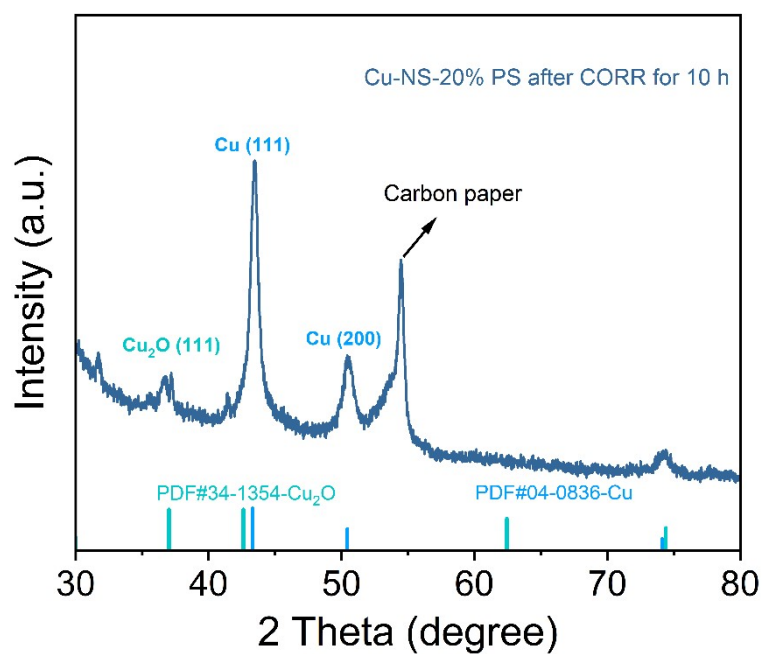


Fig. S29. XRD pattern of Cu-NS-20% PS electrode after CORR test for 10 h.

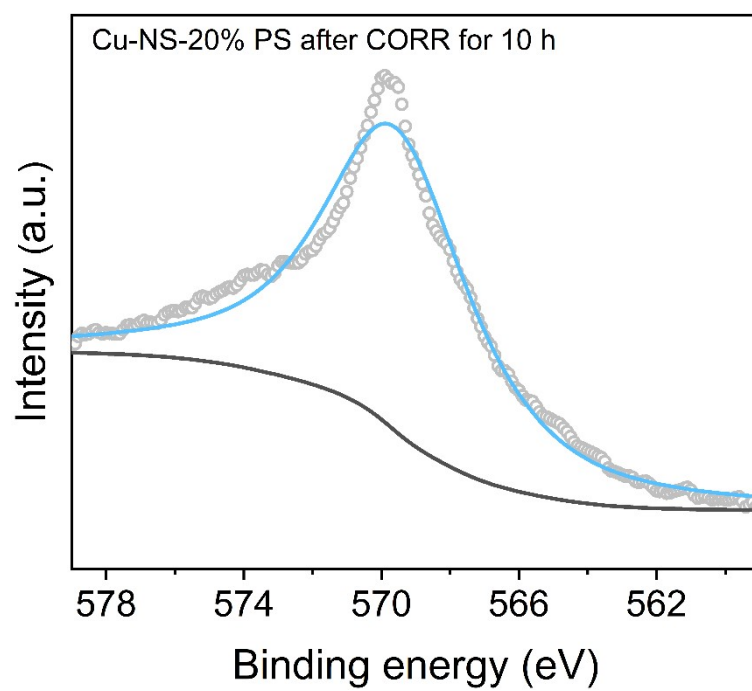


Fig. S30. Cu LMM Auger spectrum of Cu-NS-20% PS electrode after CORR for 10 h.

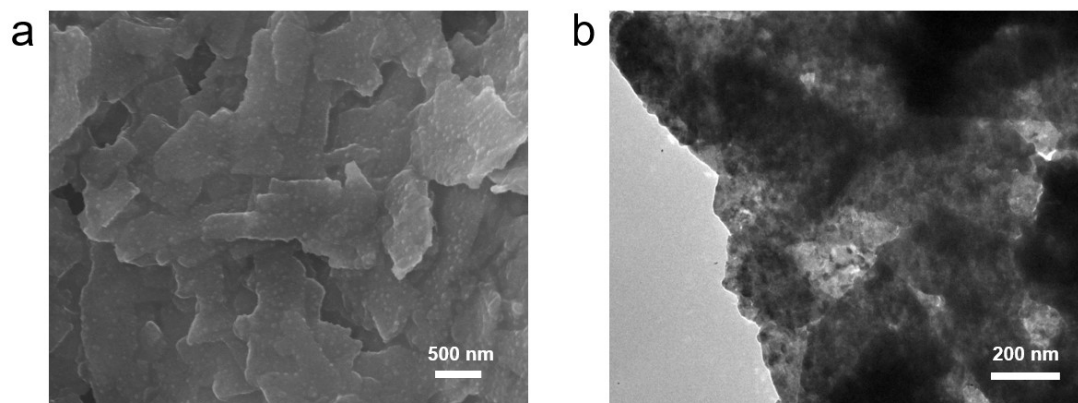


Fig. S31. SEM (a) and TEM (b) images of Cu-NS-20% PS electrode after CORR test for 10 h.

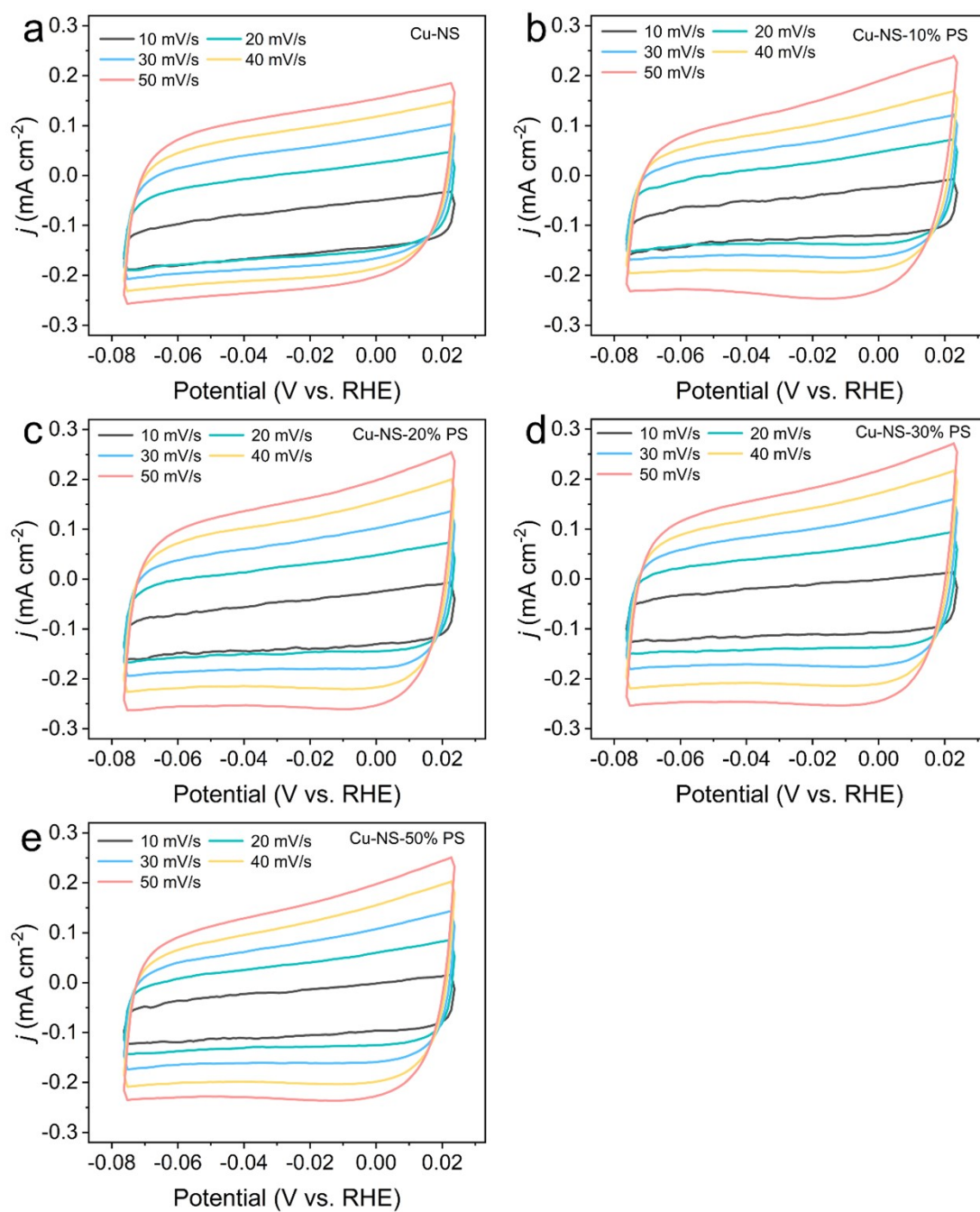


Fig. S32. Cyclic voltammetry at different scan rates: (a) Cu-NS, (b) Cu-NS-10% PS, (c) Cu-NS-20% PS, (d) Cu-NS-30% PS and (e) Cu-NS-50% PS.

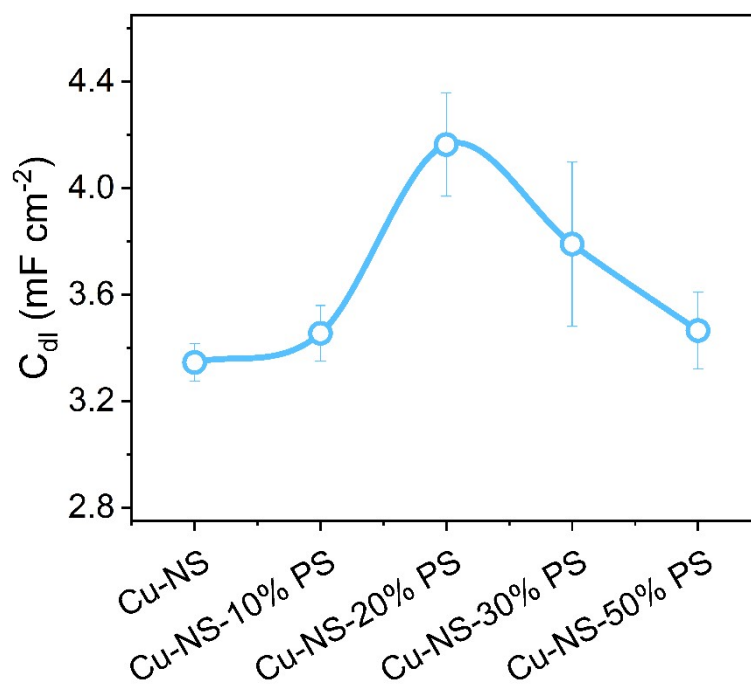


Fig. S33. Comparison of C_{dl} of Cu-NS-x% PS with different amount of PS (x = 0, 10, 20, 30 and 50).

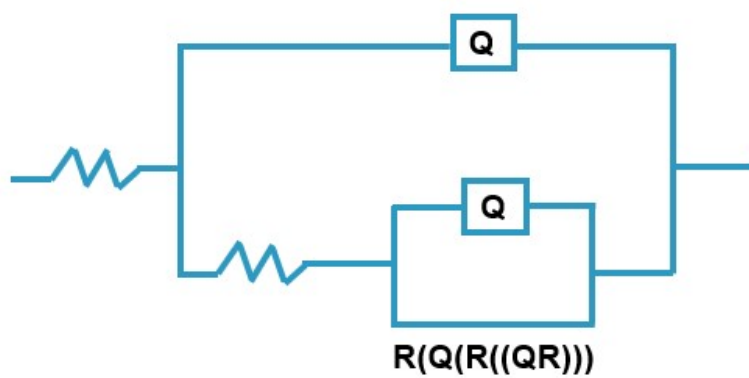


Fig. S34. Equivalent circuit diagram for EIS fitting.



Fig. S35. Picture of the custom-made high-pressure spectroelectrochemical setup for SEIRAS investigation.

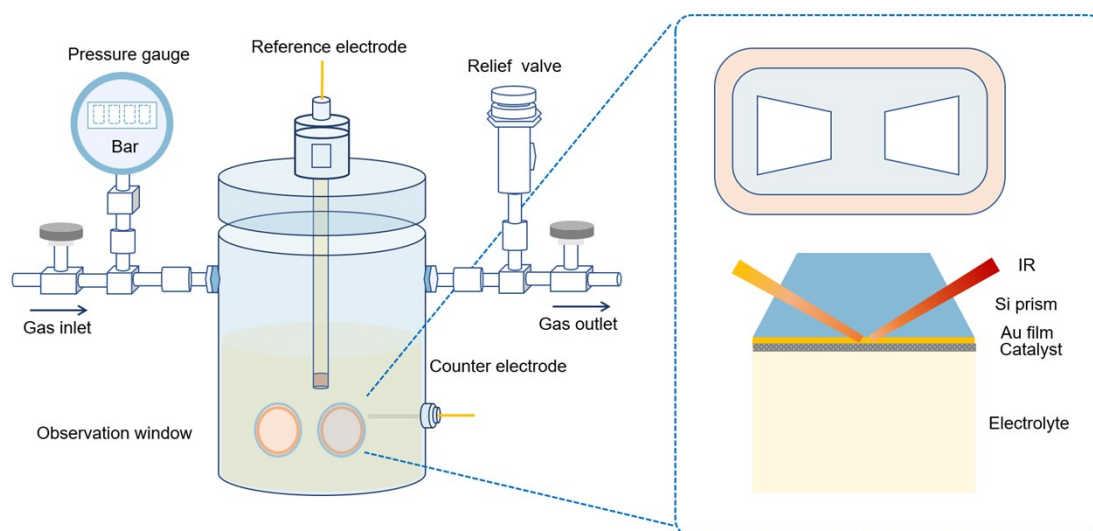


Fig. S36. Schematic diagram of the custom-made high-pressure spectroelectrochemical setup.

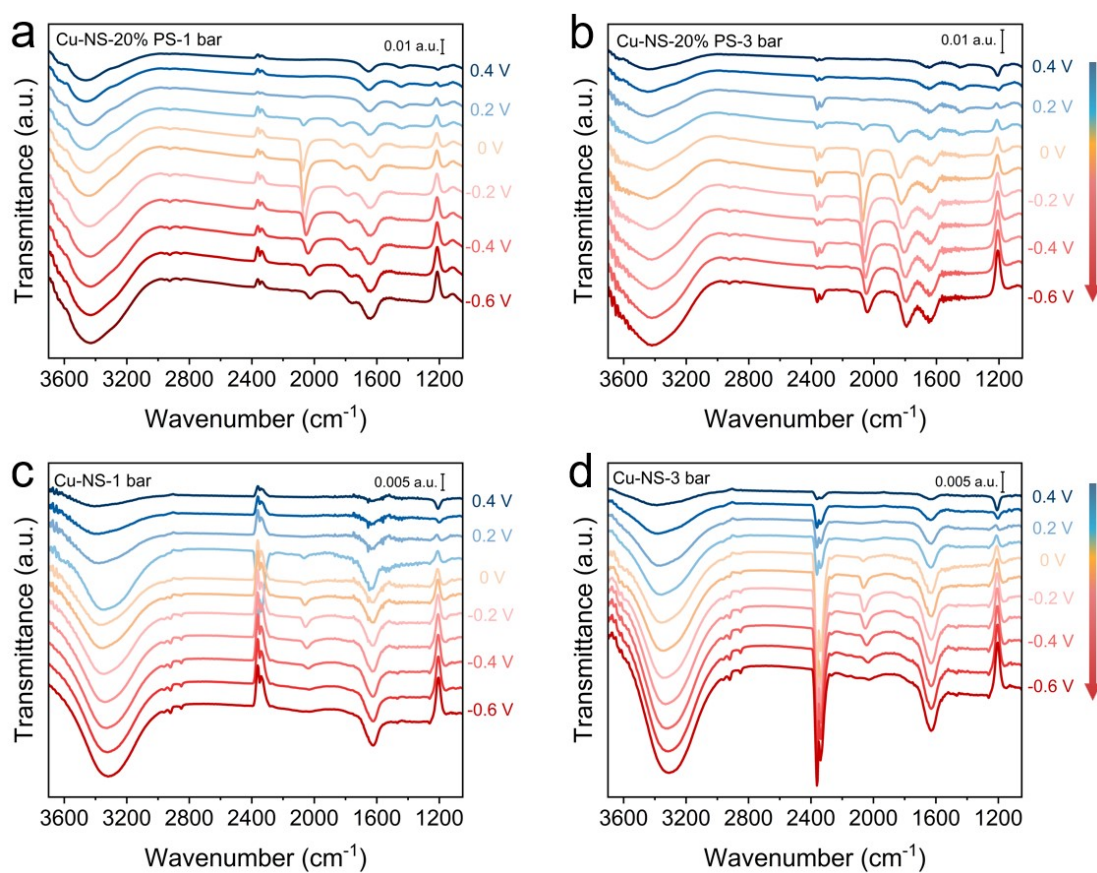


Fig. S37. *In situ* ATR-SEIRAS spectra taken by ramping down the applied potential from 0.4 to -0.6 V vs. RHE in 0.1 M KOH on Cu-NS-20% PS under (a) 1 bar CO, (b) 3 bar CO. *In situ* ATR-SEIRAS spectra taken by ramping down the applied potential from 0.4 to -0.6 V vs. RHE in 0.1 M KOH on Cu-NS under (c) 1 bar CO, (d) 3 bar CO.

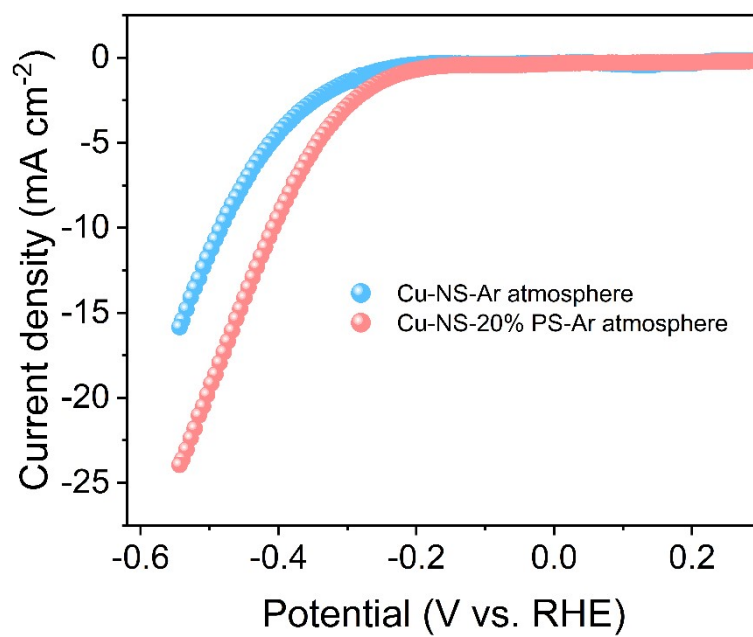


Fig. S38. The linear sweep voltammetry curve per geometric area in 1 M KOH under Ar atmosphere for the Cu-NS-20% PS and Cu-NS catalysts, respectively.

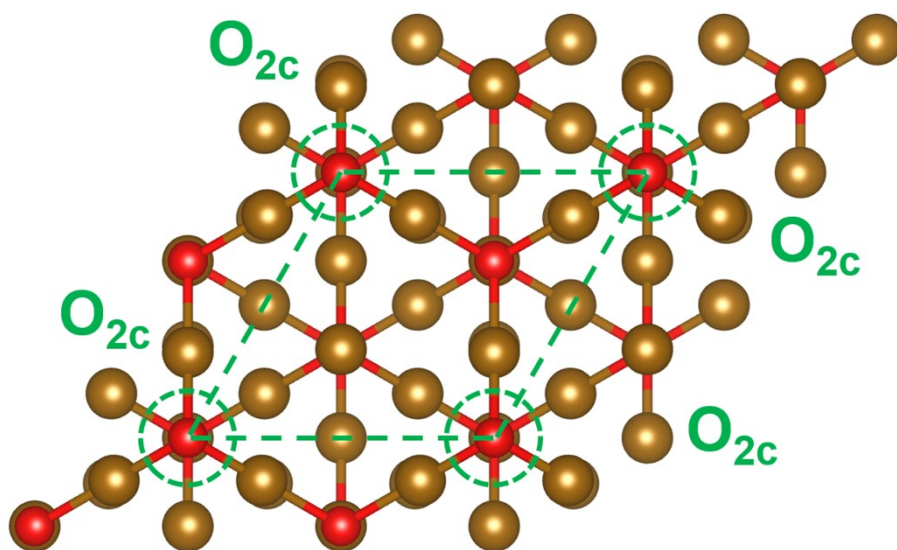


Fig. S39. The emplacement of superficial two-fold coordinated oxygen sites which upon removal of oxygen atoms become vacancies at the (111) surface of Cu_2O . These sites denoted as O_{2c} are depicted by green circles.

Each 2×2 slab of pristine (111) surface contains up to 4 superficial oxygen vacancies. Therefore, the removal of one, two or three of these oxygen atoms leads to the coverages of $\frac{1}{4}$ ML, $\frac{1}{2}$ ML and $\frac{3}{4}$ ML.

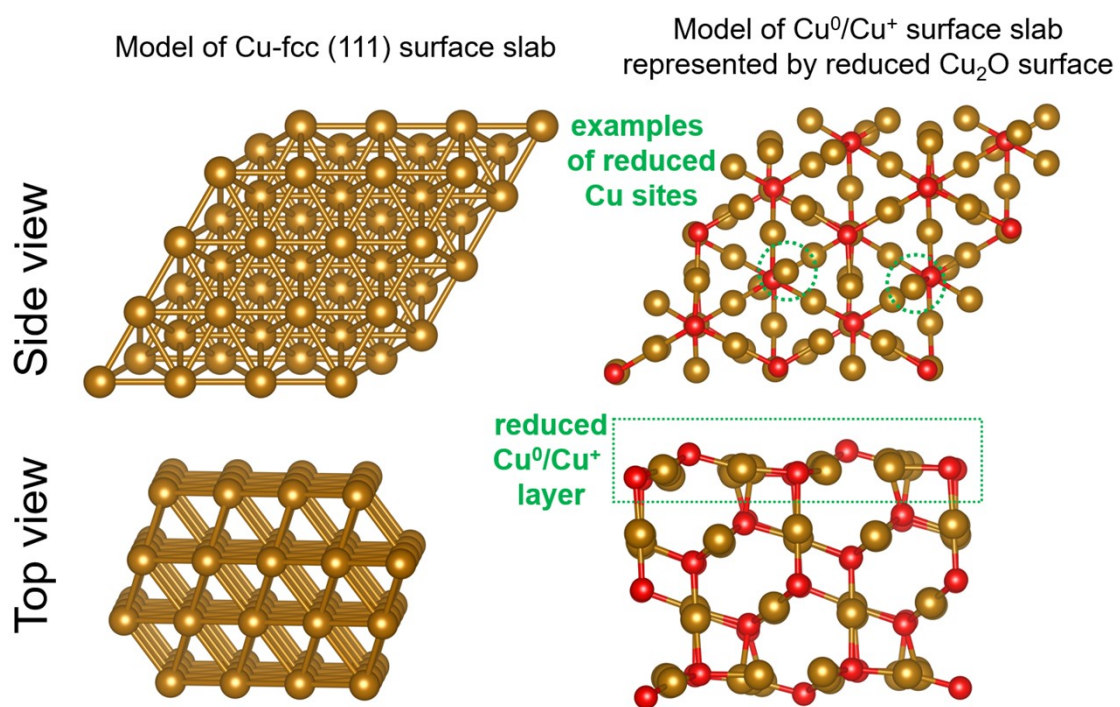


Fig. S40. Model of Cu-fcc (111) surface slab and Cu⁰/Cu⁺ surface slab represented by reduced Cu₂O surface.

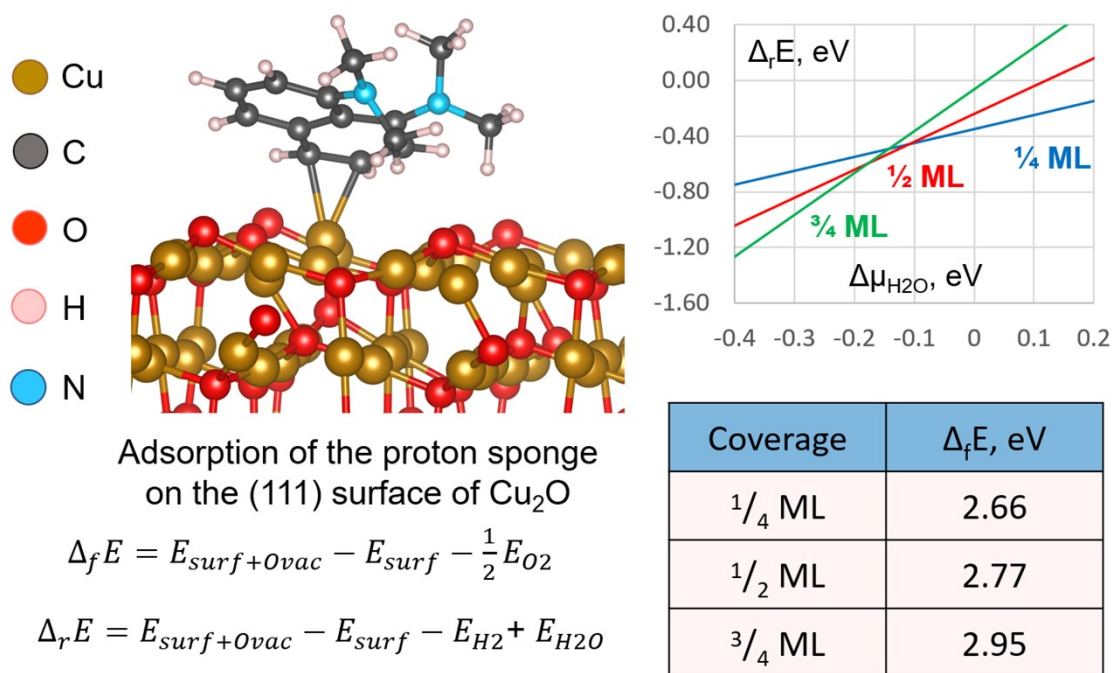


Fig. S41. Adsorption of proton sponge on the Cu_2O surface and its effect on the stabilization of the Cu^+ state.

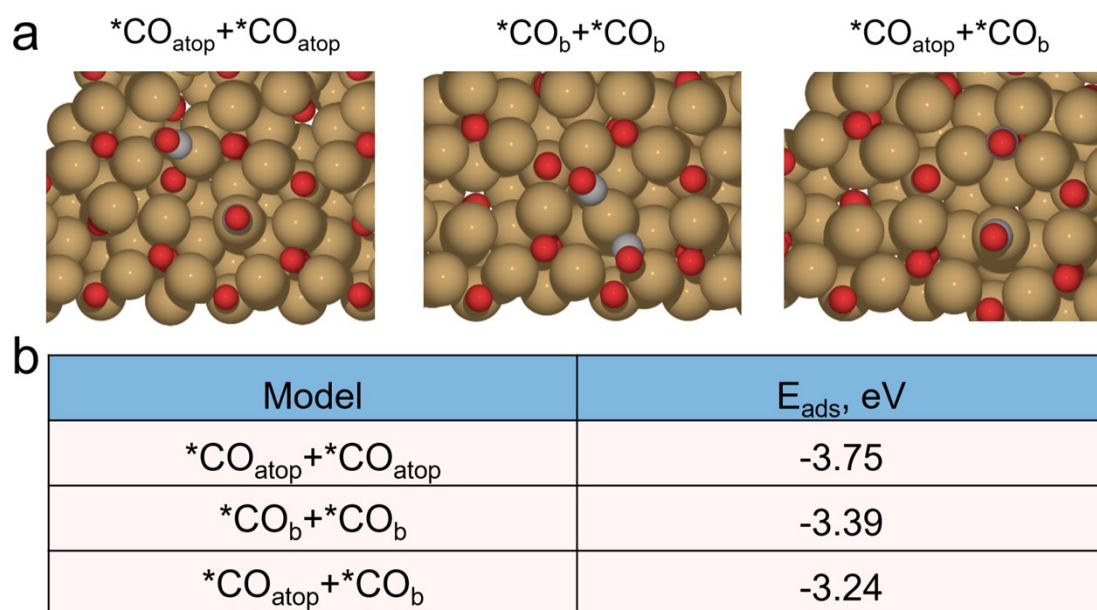


Figure S42. (a) Combinations of different $*CO$ adsorption configurations and (b) adsorption energy.

$*CO_b$ adsorption specifically occurs under high pressure, and the control sample does not show $*CO_b$ under the same conditions because DFT calculations show the $*CO_{atop}$ configuration to be the most stable.

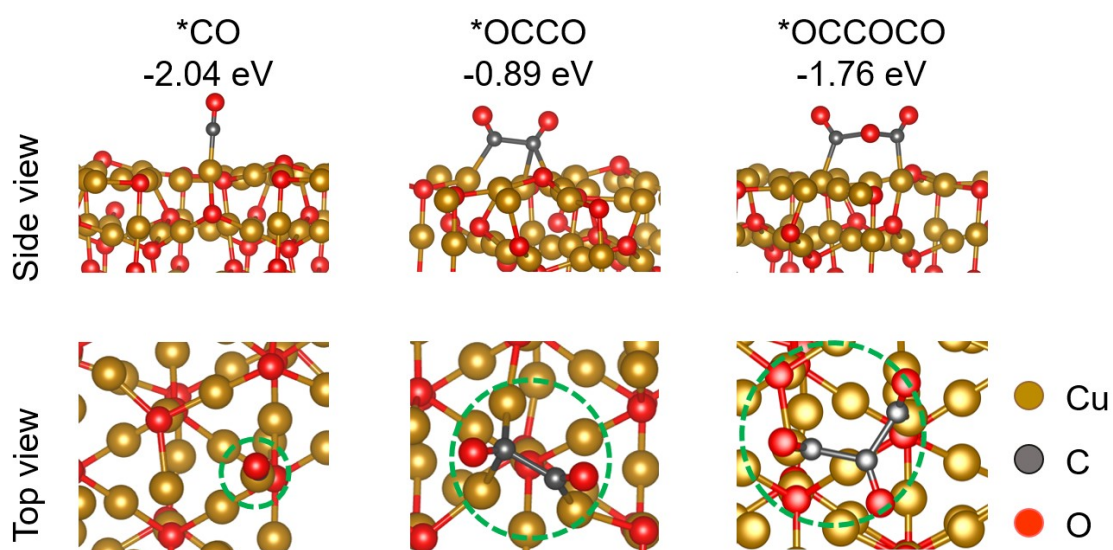


Fig. S43. Key intermediates of the propanol synthesis (C-chain growth stage) on Cu^0/Cu^+ surface.

In the DFT calculations, both $^*\text{CO}_{\text{atop}}$ and $^*\text{CO}_{\text{b}}$ participate in CO coupling to form n-propanol.

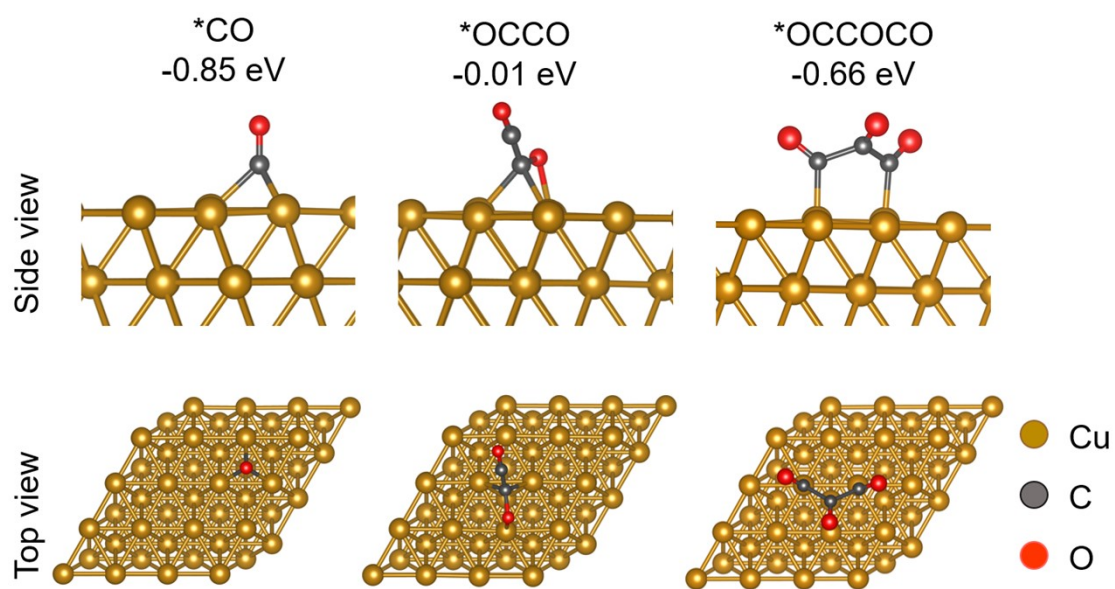


Fig. S44. Key intermediates of the propanol synthesis (C-chain growth stage) on Cu^0 (111) surface.

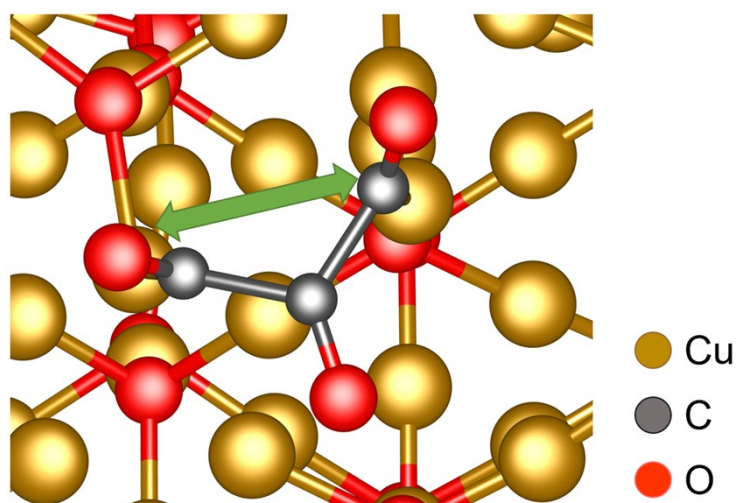
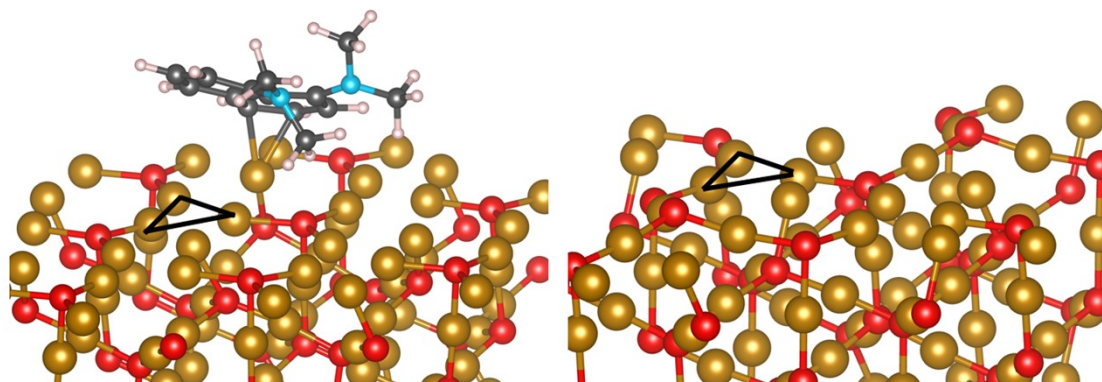


Fig. S45. Favorable topology of the copper sites in the Cu⁺/Cu⁰ system.

Cu-Cu distances on the Cu⁰/Cu⁺ surfaces



	Cu₁ – Cu₂	Cu₂ – Cu₃	Cu₁ – Cu₃
With proton sponge	2.530 Å	2.556 Å	2.537 Å
Without proton sponge	2.431 Å	2.431 Å	2.555 Å

Fig. S46. The distances of Cu-Cu in the triangle in the presence and in the absence of proton sponge.

The presence of the proton sponge at the surface makes the distances between Cu sites more homogeneous that increases the probability of triple coupling of the CO molecules, rather than formation of C₂ products. Indeed, without proton sponge in the Cu-Cu triangle there are two Cu-Cu distances that are shorter than another one, while in the presence of proton sponge all three Cu-Cu distances in the triangle are almost equal in length, that is favorable for the simultaneous CO-CO-CO coupling and pushes the reaction towards the formation of the C₃ product.

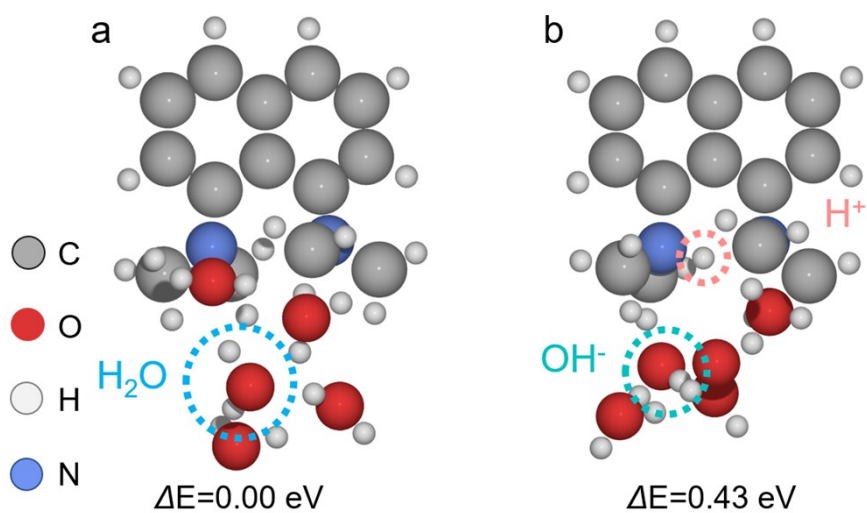


Fig. S47. (a) proton sponge and water system. (b) The system with H^+ within the proton sponge and hydrated OH^- .

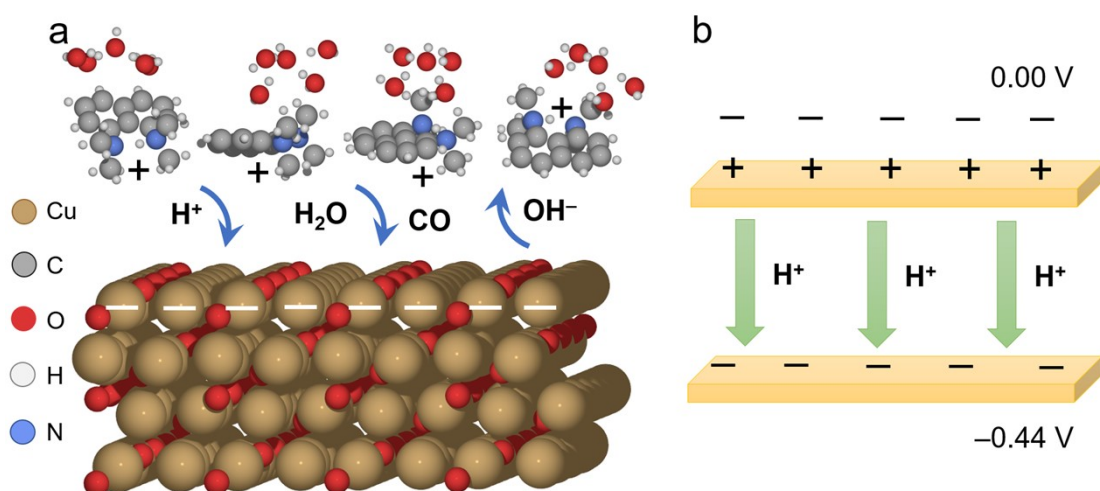


Fig. S48. (a) Schematic illustration of acting mechanism for the system with H^+ within the proton sponge and hydrated OH^- . (b) Schematic illustration for the electrochemical overpotential applied to the system during the reaction and attracted H^+ to the catalyst surface.

Table S1. Summary of CO₂/CORR performances on different Cu-based electrocatalysts for n-propanol generation.

Catalyst	FE of n-propanol	Potential (V vs. RHE)	Reaction gas	<i>j</i> _{n-propanol} (mA cm ⁻²)	Stability (hours)	Reference
Cu-NS-20% PS	44.0% ± 2.3%	-0.44	CO	-5.5@H-type cell	10	<i>This work</i>
Nanocavity Cu	21 ± 1%	-0.56	CO	-7.8@flow cell	2.4	<i>Nat. Catal.</i> , 2018, 1 , 946-951. ⁶
Fragmented Cu	20%	-0.45	CO	-8.5@flow cell	3.3	<i>Nat. Catal.</i> , 2019, 2 , 251-258. ⁷
Cu	4.2%	-	CO	-4.2@flow cell	2	<i>Energy Environ. Sci.</i> , 2022, 15 , 2470-2478. ⁸
Ag-doped Cu	33 ± 1%	-0.46	CO	-4.5@flow cell	3.3	<i>Nat. Commun.</i> , 2019, 10 , 5186. ⁹
Cu adparticles	23%	-0.47	CO	-11@flow cell	n. r.	<i>Nat. Commun.</i> , 2018, 9 , 4614. ¹⁰
NGQ/Cu-nr	27.2%	-0.7	CO	-82.3@flow cell	n. r.	<i>Angew. Chem. Int. Ed.</i> , 2020, 59 , 16459-16464. ¹¹
OD-Cu	26%	-0.42	CO	-11.7@flow cell	n. r.	<i>Nat. Catal.</i> , 2018, 1 , 748-755. ¹²
OD-Cu 2	10%	-0.4	CO	n.r.	n. r.	<i>Nature</i> , 2014, 508 , 504-507. ¹³
BCF-Cu ₂ O	19.3%	-0.45	CO	-0.85@flow cell	n. r.	<i>J. Am. Chem. Soc.</i> , 2022, 144 , 12410-12420. ¹⁴
Multi-hollow Cu ₂ O	30.2%	n. r.	CO	-12.8@flow cell	0.5	<i>Adv. Energy Mater.</i> , 2022, 12 , 2202054. ¹⁵
(Cu ₂ O@) ₂ @Cu ₂ O YSNPs	22.22%	n. r.	CO	-11.11@flow cell	5	<i>ACS Nano</i> , 2023, 17 , 8663-8670. ¹⁶
Ag-Ru-Cu	37% ± 3%	n. r.	CO	-111@MEA	108	<i>Nat. Energy</i> , 2022, 7 , 170-176. ¹⁷
Pb-Cu	46.6 ± 3%	-0.68	CO	-38@flow cell	10	<i>Nat. Commun.</i> , 2023, 14 , 4882. ¹⁸
CuAg _{5%} N _{20h}	45%	n. r.	CO	-67.5@flow cell	n. r.	<i>Angew. Chem. Int. Ed.</i> , 2023, 62 , e202310788. ¹⁹
CuAg _{5%} N _{20h}	39%	n. r.	CO	-58.5@flow cell	9	<i>Angew. Chem. Int. Ed.</i> , 2023, 62 , e202310788. ¹⁹
R-Cu/Au	37.66%	-0.53	CO	-2.52@H-type cell	n. r.	<i>J. Am. Chem. Soc.</i> , 2024, 146 , 4632-4641. ²⁰
R-Cu/Au	46.63%	-0.58	CO	-21.52@flow cell	9	<i>J. Am. Chem. Soc.</i> , 2024, 146 , 4632-4641. ²⁰
Spheric Cu/C	11.5%	-0.6	CO	-0.29@H-type cell	2	<i>ACS Catal.</i> , 2019, 9 , 4709-4718. ²¹
Cu(OD) _{0.8} Ag _{0.2}	~5%	n. r.	CO	~-5@MEA	100	<i>Nat. Commun.</i> , 2023, 14 , 698. ²²
Cu ₅ P ₂ O ₁₀	~15%	n. r.	CO	-60@MEA	42	<i>Energy Environ. Sci.</i> , 2024, 17 , 3594-3603. ²³
Cu-HDD	~15%	n. r.	CO	~-75@flow cell	5	<i>Adv. Mater.</i> , 2020, 32 , 2002382. ²⁴
Hex-2Cu-O	18.3%	-1.2	CO ₂	-9.4@flow cell	25	<i>Nat. Commun.</i> , 2022, 13 , 5122. ²⁵
CuS _x -DSV	15.4%	-1.05	CO ₂	-3.1@H-type cell	10	<i>Nat. Commun.</i> , 2021, 12 , 1580. ²⁶
CuOD-Cu	17.9%	-0.94	CO ₂	-4.61@H-type cell	150	<i>Sci. Adv.</i> , 2023, 9 , eadi6119. ²⁷

Table S2. Mole percentage of proton sponge in the CuO-NS-x% PS by the thermal gravimetric analyzer (TGA), XPS and SEM-EDX.

Catalyst	Mole percentage of proton sponge by TGA	Mole percentage of proton sponge by XPS	Mole percentage of proton sponge by SEM-EDX
CuO-NS-10% PS	0.45% mol _{PS} /mol _{CuO}	2.55% mol _{PS} /mol _{CuO}	1.25% mol _{PS} /mol _{CuO}
CuO-NS-20% PS	2.60% mol _{PS} /mol _{CuO}	2.83% mol _{PS} /mol _{CuO}	3.05% mol _{PS} /mol _{CuO}
CuO-NS-30% PS	4.64% mol _{PS} /mol _{CuO}	2.90% mol _{PS} /mol _{CuO}	3.84% mol _{PS} /mol _{CuO}
CuO-NS-50% PS	7.53% mol _{PS} /mol _{CuO}	3.26% mol _{PS} /mol _{CuO}	5.55% mol _{PS} /mol _{CuO}

Table S3. Summary of C₂₊ products distribution of CORR on different Cu-based electrocatalysts under different CO pressures.

Catalyst	FE of C ₂₊ products under lower CO pressure	FE of C ₂₊ products under higher CO pressure	Reference
Cu-NS	C ₂ H ₄ @31.8%, CH ₃ CH ₂ OH@31.1%, CH ₃ COOH@37.8%, n-propanol@18.7% at 1 bar CO	C ₂ H ₄ @16.8%, CH ₃ CH ₂ OH@22.1%, CH ₃ COOH@40.6%, n-propanol@31.9% at 3 bar CO	<i>This work</i>
Cu-NS-20% PS	C ₂ H ₄ @23.9%, CH ₃ CH ₂ OH@25.0%, CH ₃ COOH@11.1%, n-propanol@26.0% at 1 bar CO	C ₂ H ₄ @20.7%, CH ₃ CH ₂ OH@17.3%, CH ₃ COOH@21.2%, n-propanol@44.0% at 3 bar CO	<i>This work</i>
Cu/Ag-DA	C ₂ H ₄ @13.6%, CH ₃ CH ₂ OH@5.6%, CH ₃ COOH@69.1%, n-propanol@0% at 1 atm CO	C ₂ H ₄ @5.2%, CH ₃ CH ₂ OH@1.8%, CH ₃ COOH@91.2%, n-propanol@0% at 10 atm CO	<i>Nature</i> , 2023, 617 , 724-729 ²⁸
OD-Cu-1	C ₂ H ₄ @4.6%, CH ₃ CH ₂ OH@42.9%, CH ₃ COOH@13.6%, n-propanol@0% at 1 atm CO	C ₂ H ₄ @1.4%, CH ₃ CH ₂ OH@33.2%, CH ₃ COOH@16.8%, n-propanol@3.0% at 2.4 atm CO	<i>Nature</i> , 2014, 508 , 504-507 ¹³
Aggregated Cu nanoparticle	C ₂ H ₄ @~70%, CH ₃ CH ₂ OH@~25%, CH ₃ COOH@~2%, n-propanol@~6% at 5% CO	C ₂ H ₄ @~44%, CH ₃ CH ₂ OH@~19%, CH ₃ COOH@~5%, n-propanol@~30% at 100% CO	<i>Nat. Catal.</i> , 2019, 2 , 1124- 1131 ²⁹

Table S4. Experimental data of C_{dl} of Cu-NS-x% PS (x = 0, 10, 20, 30 and 50) from three independent measurements.

Catalyst	First round/C_{dl} (mF cm⁻²)	Second round/C_{dl} (mF cm⁻²)	Third round/C_{dl} (mF cm⁻²)
Cu-NS	3.46	3.29	3.29
Cu-NS-10% PS	3.60	3.46	3.31
Cu-NS-20% PS	4.47	3.94	4.08
Cu-NS-30% PS	4.05	4.04	3.29
Cu-NS-50% PS	3.45	3.68	3.27

References

1. B. Zhang, J. Zhang, M. Hua, Q. Wan, Z. Su, X. Tan, L. Liu, F. Zhang, G. Chen, D. Tan, X. Cheng, B. Han, L. Zheng and G. Mo, *J. Am. Chem. Soc.*, 2020, **142**, 13606-13613.
2. H. Miyake, S. Ye and M. Osawa, *Electrochem. Commun.*, 2002 **4**, 973-977.
3. J. P. Perdew, M. Ernzerhof and K. Burke, *J. Chem. Phys.*, 1996, **105**, 9982-9985.
4. P. Giannozzi, S. Baroni, N. Bonini, M. Calandra, R. Car, C. Cavazzoni, D. Ceresoli, G. L. Chiarotti, M. Cococcioni, I. Dabo, A. Dal Corso, S. de Gironcoli, S. Fabris, G. Fratesi, R. Gebauer, U. Gerstmann, C. Gougoussis, A. Kokalj, M. Lazzeri, L. Martin-Samos, N. Marzari, F. Mauri, R. Mazzarello, S. Paolini, A. Pasquarello, L. Paulatto, C. Sbraccia, S. Scandolo, G. Sclauzero, A. P. Seitsonen, A. Smogunov, P. Umari and R. M. Wentzcovitch, *J. Phys. Condens. Matter*, 2009, **21**, 395502.
5. K. F. Garrity, J. W. Bennett, K. M. Rabe and D. Vanderbilt, *Comp. Mater. Sci.*, 2014, **81**, 446-452.
6. T.-T. Zhuang, Y. Pang, Z.-Q. Liang, Z. Wang, Y. Li, C.-S. Tan, J. Li, C. T. Dinh, P. De Luna, P.-L. Hsieh, T. Burdyny, H.-H. Li, M. Liu, Y. Wang, F. Li, A. Proppe, A. Johnston, D.-H. Nam, Z.-Y. Wu, Y.-R. Zheng, A. H. Ip, H. Tan, L.-J. Chen, S.-H. Yu, S. O. Kelley, D. Sinton and E. H. Sargent, *Nat. Catal.*, 2018, **1**, 946-951.
7. Y. Pang, J. Li, Z. Wang, C.-S. Tan, P.-L. Hsieh, T.-T. Zhuang, Z.-Q. Liang, C. Zou, X. Wang, P. De Luna, J. P. Edwards, Y. Xu, F. Li, C.-T. Dinh, M. Zhong, Y. Lou, D. Wu, L.-J. Chen, E. H. Sargent and D. Sinton, *Nat. Catal.*, 2019, **2**, 251-258.
8. M. Ma, W. Deng, A. Xu, D. Hochfilzer, Y. Qiao, K. Chan, I. Chorkendorff and B. Seger, *Energy Environ. Sci.*, 2022, **15**, 2470-2478.
9. X. Wang, Z. Wang, T. T. Zhuang, C. T. Dinh, J. Li, D. H. Nam, F. Li, C. W. Huang, C. S. Tan, Z. Chen, M. Chi, C. M. Gabardo, A. Seifitokaldani, P. Todorovic, A. Proppe, Y. Pang, A. R. Kirmani, Y. Wang, A. H. Ip, L. J. Richter, B. Scheffel, A. Xu, S. C. Lo, S. O. Kelley, D. Sinton and E. H. Sargent, *Nat. Commun.*, 2019, **10**, 5186.
10. J. Li, F. Che, Y. Pang, C. Zou, J. Y. Howe, T. Burdyny, J. P. Edwards, Y. Wang, F. Li, Z. Wang, P. De Luna, C. T. Dinh, T. T. Zhuang, M. I. Saidaminov, S. Cheng, T. Wu, Y. Z. Finprock, L. Ma, S. H. Hsieh, Y. S. Liu, G. A. Botton, W. F. Pong, X. Du, J. Guo, T. K. Sham, E. H. Sargent and D. Sinton, *Nat. Commun.*, 2018, **9**, 4614.
11. C. Chen, X. Yan, S. Liu, Y. Wu, Q. Wan, X. Sun, Q. Zhu, H. Liu, J. Ma, L. Zheng, H. Wu and B. Han, *Angew. Chem. Int. Ed.*, 2020, **59**, 16459-16464.
12. M. Jouny, W. Luc and F. Jiao, *Nat. Catal.*, 2018, **1**, 748-755.
13. C. W. Li, J. Ciston and M. W. Kanan, *Nature*, 2014, **508**, 504-507.

14. J. Liu, F. You, B. He, Y. Wu, D. Wang, W. Zhou, C. Qian, G. Yang, G. Liu, H. Wang, Y. Guo, L. Gu, L. Feng, S. Li and Y. Zhao, *J. Am. Chem. Soc.*, 2022, **144**, 12410-12420.
15. G. Wu, Y. Song, Q. Zheng, C. Long, T. Fan, Z. Yang, X. Huang, Q. Li, Y. Sun, L. Zuo, S. Lei and Z. Tang, *Adv. Energy Mater.*, 2022, **12**, 2202054.
16. H. Du, L. X. Liu, P. Li, Q. Min, S. Guo and W. Zhu, *ACS Nano*, 2023, **17**, 8663-8670.
17. X. Wang, P. Ou, A. Ozden, S.-F. Hung, J. Tam, C. M. Gabardo, J. Y. Howe, J. Sisler, K. Bertens, F. P. García de Arquer, R. K. Miao, C. P. O'Brien, Z. Wang, J. Abed, A. S. Rasouli, M. Sun, A. H. Ip, D. Sinton and E. H. Sargent, *Nat. Energy*, 2022, **7**, 170-176.
18. W. Niu, Z. Chen, W. Guo, W. Mao, Y. Liu, Y. Guo, J. Chen, R. Huang, L. Kang, Y. Ma, Q. Yan, J. Ye, C. Cui, L. Zhang, P. Wang, X. Xu and B. Zhang, *Nat. Commun.*, 2023, **14**, 4882.
19. H. Phong Duong, J. G. Rivera de la Cruz, N. H. Tran, J. Louis, S. Zanna, D. Portehault, A. Zitolo, M. Walls, D. V. Peron, M. W. Schreiber, N. Menguy and M. Fontecave, *Angew. Chem. Int. Ed.*, 2023, **62**, e20231078.
20. C. Long, K. Wan, Y. Chen, L. Li, Y. Jiang, C. Yang, Q. Wu, G. Wu, P. Xu, J. Li, X. Shi, Z. Tang and C. Cui, *J. Am. Chem. Soc.*, 2024, **146**, 4632-4641.
21. J. Li, K. Chang, H. Zhang, M. He, W. A. Goddard, J. G. Chen, M.-J. Cheng and Q. Lu, *ACS Catal.*, 2019, **9**, 4709-4718.
22. J. Li, H. Xiong, X. Liu, D. Wu, D. Su, B. Xu and Q. Lu, *Nat. Commun.*, 2023, **14**, 698.
23. J. Sang, T. Liu, P. Wei, H. Li, C. Liu, Y. Wang, Y. Rong, Q. Wang, G. Wang and X. Bao, *Energy Environ. Sci.*, 2024, **17**, 3594-3603.
24. C. Zhao, G. Luo, X. Liu, W. Zhang, Z. Li, Q. Xu, Q. Zhang, H. Wang, D. Li, F. Zhou, Y. Qu, X. Han, Z. Zhu, G. Wu, J. Wang, J. Zhu, T. Yao, Y. Li, H. J. M. Bouwmeester and Y. Wu, *Adv. Mater.*, 2020, **32**, e2002382.
25. B. Yang, L. Chen, S. Xue, H. Sun, K. Feng, Y. Chen, X. Zhang, L. Xiao, Y. Qin, J. Zhong, Z. Deng, Y. Jiao and Y. Peng, *Nat. Commun.*, 2022, **13**, 5122.
26. C. Peng, G. Luo, J. Zhang, M. Chen, Z. Wang, T. K. Sham, L. Zhang, Y. Li and G. Zheng, *Nat. Commun.*, 2021, **12**, 1580.
27. C. Long, X. Liu, K. Wan, Y. Jiang, P. An, C. Yang, G. Wu, W. Wang, J. Guo, L. Li, K. Pang, Q. Li, C. Cui, S. Liu, T. Tan and Z. Tang, *Sci. Adv.*, 2023, **9**, eadi6119.
28. J. Jin, J. Wicks, Q. Min, J. Li, Y. Hu, J. Ma, Y. Wang, Z. Jiang, Y. Xu, R. Lu, G. Si, P. Papangelakis, M. Shakouri, Q. Xiao, P. Ou, X. Wang, Z. Chen, W. Zhang, K. Yu, J. Song, X. Jiang, P. Qiu, Y. Lou, D. Wu, Y. Mao, A. Ozden, C. Wang, B. Y. Xia, X. Hu, V. P. Dravid, Y. M. Yiu, T. K. Sham, Z. Wang, D. Sinton, L. Mai, E. H. Sargent and Y. Pang, *Nature*, 2023, **617**, 724-729.
29. J. Li, Z. Wang, C. McCallum, Y. Xu, F. Li, Y. Wang, C. M. Gabardo, C.-T. Dinh, T.-T. Zhuang, L. Wang, J. Y. Howe, Y. Ren, E. H. Sargent and D. Sinton, *Nat. Catal.*, 2019, **2**, 1124-1131.